A Preliminary Study on a Synergistic Assimilation Scheme for Multi-band Satellite Soil Moisture Data

Xuesong Bai[1,2], Zhaohui Lin[1,3], Zhengkun Qin[1,2], Juan Li[4,5]

[1]Collaborative Innovation Center on Forecast and Evaluation of Meteorological Disasters, Nanjing University of Information Science and Technology, Nanjing, 210044, China; 202311010004@nuist.edu.cn (X.B.)
[2]State Key Laboratory of Climate System Prediction and Risk Management, Nanjing University of Information Science and Technology, Nanjing, 210044, China
[3]International Center for Climate and Environment Sciences, Institute of Atmospheric Physics, Chinese Academy of Sciences, Beijing, 100029, China
[4]CMA Earth System Modeling and Prediction Centre, Beijing, 100081, China; lj@cma.gov.cn
[5]State Key Laboratory of Severe Weather, Chinese Academy of Meteorological Sciences, Beijing, 100081, China

Correspondence to: Zhaohui Lin (lzh@mail.iap.ac.cn); Zhengkun Qin (qzk_0@nuist.edu.cn)

Abstract. Soil moisture retrievals from satellite sensors operating at different microwave frequencies provide diverse and complementary data sources for assimilation. However, fully exploiting the advantages of each frequency band while increasing the volume of assimilated observations remains a challenge. This study assimilates soil-moisture retrievals from three dominant-frequency instruments—SMAP (Soil Moisture Active–Passive), ASCAT (Advanced Scatterometer), and MWRI (Microwave Radiation Imager)—into the Common Land Model (CoLM) via the Simplified Extended Kalman Filter (SEKF). On the basis of a systematic assessment of the disparate impacts of each single-band product, we propose and test a synergistic multi-satellite assimilation framework that optimally combines the complementary information inherent in the multi-frequency observations. Results show that assimilating soil-moisture retrievals improves the accuracy of the CoLM land-surface model; nevertheless, the effectiveness of each product varies with vegetation type. Analyses of simultaneous multi-source assimilation indicate that retrieval uncertainties associated with frequency-dependent differences in vegetation penetration capability are the dominant factor controlling the effectiveness of joint assimilation. When SMAP and ASCAT products are already ingested, the additional introduction of MWRI data over low-stature vegetation, where vegetation attenuation is relatively weak, provides complementary information and further enhances the joint assimilation performance. Validation against in-situ observations across China demonstrates that the largest improvements occur in the central and western parts of the country: compared with the open-loop simulation, the domain-mean correlation coefficient rises by about 0.25, while the error declines from 0.068 to 0.058 m^3/m^3. This indicates that improvements from multi-sensor assimilation stem not only from increased data volume but also from the complementary characteristics of the assimilated products. These findings provide valuable insights into the design of synergistic multi-sensor land data assimilation systems and contribute to improving land surface modeling, as well as weather and climate prediction accuracy.

Deleted: [2]
Deleted: [3]
Deleted: [4]
Formatted: Not Superscript/ Subscript
Formatted: (Asian) Chinese (China), Not Superscript/ Subscript
Deleted: State Key Laboratory of Climate System Prediction and Risk Management, Nanjing University of Information Science and Technology, Nanjing, 210044, China
Deleted: ; qzk_0@nuist.edu.cn (Z.Q.)
Formatted: Font: (Asian) Times New Roman, Superscript
Formatted: Font: (Asian) SimSun
Deleted: [2]
Deleted: [3]
Deleted: [4]
Formatted: Font: (Asian) +Body Asian (SimSun), (Asian) Chinese (China)
Deleted: ,
Deleted: w
Deleted: further enhances the joint assimilation performance

1 Introduction

Soil moisture is a critical component of the terrestrial water and energy cycles, exerting strong influences on agricultural productivity, weather and climate prediction, water resources management, and climate change (Seneviratne et al., 2010; Taylor, 2015; Wanders et al., 2019b; Zhang et al., 2002). In the climate system, soil moisture primarily modulates the partitioning of surface sensible and latent heat fluxes, thereby directly influencing the energy exchange processes involved in land–atmosphere interactions (Lin et al., 2010; Zhan and Lin, 2011; Zhou et al., 2020). Because soil moisture has memory properties, soil moisture anomalies can persist from weeks to months (Koster et al., 2020; Zhan et al., 2020). This provides a crucial source of predictability for sub-seasonal to seasonal forecasts, particularly in the context of extreme events such as droughts and heatwaves (Zhou et al., 2019). In weather systems, soil moisture changes the thermodynamic structure of the near-surface atmospheric boundary layer, which influencing precipitation patterns. It also plays a critical role in triggering deep convection by modulating atmospheric stability (Taylor, 2015; Wanders et al., 2019a).

Land surface models (LSMs) provide one of the important tools for estimating soil moisture with high spatiotemporal continuity. Improving LSM accuracy is essential for producing reliable soil moisture estimates, advancing understanding of land–atmosphere interactions, and enhancing the skill of weather and climate forecasts in coupled land–atmosphere modeling systems (Dai et al., 2003; Lawrence et al., 2019). Optimizing initial conditions for LSM is a crucial method to improve forecast skills of the numerical weather and climate models. Through data assimilation combined with soil moisture observations, one can obtain initial conditions that are closest enough to the ground truth and suitable for the model, however, the effectiveness of data assimilation improvements primarily depends on the accuracy of observational data.

The high spatial heterogeneity of soil moisture makes it difficult to comprehensively represent regional or global conditions based solely on limited in-situ data (Dorigo et al., 2021). Over the past few decades, satellite-based microwave remote sensing of soil moisture has made significant progress, becoming the primary source for soil moisture observations. Microwave sensors can penetrate clouds and atmospheric aerosols, enabling the acquisition of surface information under most weather conditions. Differences in the dielectric properties of wet and dry soils enable the retrieval of soil moisture. Using microwave observations across different frequency bands, various soil moisture products have been developed. Passive microwave instruments that can be used for soil moisture retrieval typically operate in the X-, C-, and L-band frequencies, such as the X-band MWRI (Kang et al., 2021; Zhu et al., 2019), C-band SMMR (Njoku et al., 1980), AMSR-E (Njoku et al., 2003), AMSR2 (Parinussa et al., 2015), and the L-band SMOS (Kerr et al., 2012). Active microwave sensors mainly include the C-band scatterometry, such as AMI Scatterometry (Zribi, 2003) and ASCAT (Bartalis et al., 2007; Zhao et al., 2021), as well as Synthetic Aperture Radar (SAR) systems, such as Sentinel-1 (Paloscia et al., 2013). With growing interest in satellite remote sensing, many polar-orbiting meteorological satellites have been launched, forming a global collaborative observation network (Peng et al., 2021; Piepmeier et al., 2017).

Deleted: primary

Deleted: means

Formatted: Space Before: 1 line

Deleted: ¶

Deleted: .

Deleted: T

Deleted: te

Deleted: Although tThe International Soil Moisture Network (ISMN) integrates in situ measurements from multiple countries to provide long-term time series of multi-layer soil moisture (Dorigo et al., 2021).,

Deleted: t

Deleted: ¶

Deleted: continuous, large-scale

Deleted: data

Deleted: e

Deleted: e

Deleted: ,

Deleted: and

Deleted: SAR

Deleted: countries

Deleted: polar-orbiting meteorological satellites

Formatted: Font: (Default) Times New Roman, (Asian) Times New Roman

Deleted: Furthermore, the SMAP satellite combines L-band active and passive microwave sensing to further enhance the accuracy of soil moisture retrieval (Entekhabi et al., 2010). However, its active radar ceased operations on 7 July 2015, a few months after launch, leaving its L-band passive radiometer as the primary instrument for ongoing soil moisture products.

Considerable progress has been achieved in data assimilation studies using various satellite-retrieved datasets (Draper et al., 2009; Kumar et al., 2006, 2009, 2014; Lin et al., 2017; Liu et al., 2013; Santanello et al., 2016; Draper and Reichle, 2015; Liu and Mishra, 2017; Brocca et al., 2012; Shan et al., 2024; Wanders et al., 2019b; Reichle et al., 2019; Carrera et al., 2019; Tian et al., 2023; Shen et al., 2024). As the variety of satellite-retrieved products keeps expanding, the joint assimilation of multiple satellite datasets has become a key research target. Atmospheric data assimilation studies have shown that combining observations from multiple satellites with complementary orbits and sensing characteristics can increase coverage by more than 20%, enhancing assimilation performance and improving numerical weather prediction (Zapotocny et al., 2007; Chambon et al., 2023; Li et al., 2024;). Similarly, the joint assimilation of multiple satellite observations has been widely explored in land applications (Khaki et al., 2019; Kolassa et al., 2017; Seo et al., 2021). Draper et al. (2012) assimilated passive and active microwave soil moisture retrievals and reported improved estimates. Lievens et al. (2017) further combined SMAP and Sentinel-1 observations and found that the joint assimilation scheme performed better. Girotto et al. (2019) assimilated SMOS brightness temperatures together with GRACE observations to improve the estimates of soil moisture, groundwater, and runoff. The ESA-CCI project has likewise explored the integration of multiple satellite retrieval products to generate more consistent and higher-quality global datasets, primarily through the development of dynamic weighting schemes based on Triple Collocation (TC) error variance estimation (Dorigo et al., 2017; Gruber et al., 2019). All these previous studies have demonstrated that using multiple datasets can improve the accuracy of soil moisture estimation.

Due to discrepancies in satellite orbits and instrumental frequency settings among different platforms, the quality of soil moisture products retrieved from observations of various sensors differs significantly. The L-band SMAP radiometer, the C-band ASCAT scatterometry, and the X-band MWRI aboard the FY-3 satellites provide soil-moisture observations with distinct frequency-dependent characteristics. The sensitivity of different microwave frequencies (L-, C-, and X-bands) to soil moisture varies with vegetation, surface roughness, and soil properties, leading to differences in retrieval accuracy and assimilation performance. For example, compared with high-frequency bands, L-band sensors such as SMOS and SMAP possess superior physical penetration capabilities, which allow them to effectively penetrate the vegetation canopy and acquire soil information. However, in regions with dense vegetation cover, specifically when the vegetation water content (VWC) exceeds 5 kg/m², the capacity to effectively retrieve surface information remains significantly limited (Entekhabi et al., 2010; Kerr et al., 2010). Compared with longer wavelengths, C-band observations generally exhibit limited vegetation penetration capabilities. Nevertheless, the ASCAT scatterometry benefits from its multi-incidence-angle viewing geometry and a change-detection algorithm that relies on long-term time series. These features enable reliable detection of soil moisture dynamics in regions with moderate vegetation density and relatively slow vegetation changes (Wagner et al., 2013; Chen et al., 2018).

Furthermore, retrieval accuracy is influenced by environmental factors. Although complex terrain poses a universal challenge to all microwave observations, its impact on active microwave sensors, particularly SAR, is more severe because of their high sensitivity to local incidence angle variations and geometric distortions. In contrast, the shorter wavelength of FY-3 MWRI

Deleted:). AMSR retrieval data have been widely used in assimilation studies with LSM such as GEOS/Catchment and CLM4.5, significantly improving the simulation accuracy of variables like soil moisture, evapotranspiration, and surface runoff (

Deleted:). Many studies based on the Ensemble Kalman Filter (EnKF) have demonstrated the positive impact of assimilating ASCAT-retrieved soil moisture on land surface and flood prediction models

Deleted: (

Deleted:). The official SMAP Level-4 soil moisture product provides a continuous global dataset by assimilating SMAP brightness temperatures into the Catchment land surface model (

Deleted:). This assimilation approach has also proven effective in numerical weather prediction. For example,

Deleted: (

Deleted:) assimilated SMAP L-band brightness temperatures into the Canadian Land Data Assimilation System (CaLDAS) and reported clear improvements in short-range warm-season forecasts, particularly for 2-m dewpoint temperatures.

Deleted: (

Deleted:) demonstrated that assimilation of SMAP products not only enhanced land surface model forecasts but also improved parameter estimation. Additionally,

Deleted: (

Deleted: employed an image-based data assimilation approach to enhance the spatial distribution characteristics of soil moisture over inland East Asia.

Deleted: best

Deleted: ,

Deleted: ing

Deleted: P

Deleted: show

Deleted: accuracy

Formatted: Font: (Default) Times New Roman, (Asian) Times New Roman, 10 pt, Font color: Auto

Deleted: ¶
Depending on the instrument bands and orbital characteristics, the strengths and weaknesses of various soil moisture products differ significantly.

Deleted: scatterometer

Deleted: Passive microwave products offer excellent temporal coverage but suffer from coarse spatial resolution. Conversely, while Synthetic Aperture Radar (SAR) products provide high spatial resolution, their temporal coverage is limited. The Scatterometer (ASCAT) strikes a balance with high temporal coverage and ... [1]

Deleted: , t

Deleted: scatterometer

Formatted: Space Before: 1 line

Deleted: . X-band sensors perform well over bare soil but su ... [2]

makes it more sensitive to vegetation structure changes. MWRI products can provide useful complementary information in sparse-vegetation or bare-soil areas, whereas their accuracy may decrease under moderate to dense vegetation cover because of stronger vegetation scattering (Kang et al., 2021; Yao et al., 2023).

Although data assimilation integrating observations from multiple satellites has received increasing attention, relatively few studies have focused on multi-satellite assimilation that explicitly incorporates X-band observations. China has launched several Fengyun-3 (FY-3) polar-orbiting meteorological satellites. Among the currently operating FY-3 satellites, FY-3D, FY-3F, FY-3G, and FY-3H carry microwave imagers, including MWRI/MWRI-II and MWRI-RM, with X-band channels, providing abundant retrieval products derived from X-band microwave observations. FY-3 MWRI has a wider observational swath than L-band SMAP and C-band ASCAT, providing broader coverage. The increasing availability of these products creates new opportunities for joint assimilation. However, additional observations do not necessarily improve assimilation performance. The weak vegetation penetration of X-band signals can increase retrieval uncertainty under dense canopies.

Therefore, this study explicitly incorporates X-band data, and quantifies the vegetation-type-dependent heterogeneity in the assimilation efficacy of diverse satellite retrievals, thereby delineating the relative advantages associated with each spectral band. Based on this insight, a vegetation-aware multi-satellite data-assimilation framework is formulated to effectively screen and select observations with complementary potential under different vegetation conditions. This design aims to reduce anti-synergistic behavior arising from observational conflicts and improve forecast skills of the model.

The remainder of this paper is organized as follows. Section 2 details the data used in this study. Section 3 describes the CoLM, the SEKF method, and the corresponding experimental design. Section 4 presents and discusses the numerical results in detail. Finally, Section 5 summarizes the main conclusions of the study.

2 Datasets

2.1 Satellite datasets

Informed by the complementary strengths of active and passive microwave sensing at divergent frequencies, this study assimilates soil-moisture retrievals from three mainstream sensors: the U.S. Soil Moisture Active Passive (SMAP), the European Advanced Scatterometer (ASCAT), and China's Microwave Radiation Imager (MWRI). The data period covers June to August 2022, and the observations were aggregated to a daily timescale before assimilation.

This study utilized the Soil Moisture Active Passive (SMAP) Level-2 Enhanced Passive Soil Moisture product (L2_SM_P_E) provided by the U.S. National Snow and Ice Data Center (NSIDC) (O'Neill et al., 2023). Launched in January 2015, the SMAP satellite has been continuously providing global radiometer observations since April 2015. It operates in a sun-synchronous orbit with an L-band (1.41 GHz) radiometer. The descending and ascending overpasses occur at approximately 6:00 AM and

Deleted: With growing interest in satellite remote sensing, many countries have launched polar-orbiting meteorological satellites carrying microwave imagers, forming a global collaborative observation network (Peng et al., 2021; Piepmeier et al., 2017). Atmospheric data assimilation studies have shown that combining observations from multiple satellites with complementary orbits and sensing characteristics can increase coverage by more than 20%, enhancing assimilation performance and improving numerical weather prediction (Chambon et al., 2023; Li et al., 2024; Zapotocny et al., 2007). Similarly, the joint assimilation of multiple satellite observations has been widely explored in land applications (Khaki et al., 2019; Kolassa et al., 2017; Seo et al., 2021). Draper et al. (2012) assimilated passive and active microwave soil moisture retrievals and reported improved estimates. Lievens et al. (2017) further combined SMAP and Sentinel-1 observations and found that the joint assimilation scheme performed best. Girotto et al. (2019) assimilated SMOS brightness temperatures together with GRACE observations, improving estimates of soil moisture, groundwater, and runoff. The ESA-CCI project has likewise explored the integration of multiple satellite retrieval products to generate more consistent and higher-quality global datasets, primarily through the development of dynamic weighting schemes based on Triple Collocation (TC) error variance estimation (Dorigo et al., 2017; Gruber et al., 2019). Previous studies show that using multiple datasets can improve soil moisture estimation accuracy. ¶

Formatted: Font: (Asian) Times New Roman

Deleted: Although observation weights derived from retrieval errors can reduce the influence of highly uncertain observations, tIt therefore remains unclear whether X-band observations complement observations at other frequencies or degrade assimilation performance under different vegetation conditions.

Deleted: Therefore, how to effectively integrate X-band products with products from other frequency bands remains an important research direction that requires further investigation.¶
However, the assimilation of X-band products also faces its own challenges. X-band retrievals are more sensitive to near-surface conditions and more susceptible to vegetation effects than L-band or C-band products. Such differences remain important despite advances in retrieval algorithms, the intrinsic physical properties of the instruments remain (Dorigo et al., 2010). The key distinction lies in vegetation penetration, under sparse vegetation or bare soil conditions, microwave attenuation by the vegetation canopy is typically minimal. Consequently, L-band (e.g., SMAP), C-band (e.g., ASCAT), and X-band (e.g., FY-3 MWRI) sensors all exhibit high sensitivity to variations in near-surface soil moisture (Jackson and Schmugge, 1991). In regions with low to moderate vegetation density, such as croplands and grasslands, vegetation scattering and attenuation begin to affect microwave signals. Although L-band sensors generally provide superior vegetation penetration, ASCAT can still achieve stable soil moisture retrieval accuracy in many of these areas, owing to its multi-angle viewing geometries and time-series-based change detection algorithms. In high-density vegetation regions such as forests, scattering and attenuation become dominant, causing a pronounced loss of shorter wavelength bands, specifically C-band and higher frequencies, to soil moisture (Owe et al., 2001). While C-band products require external vegetation corrections, L-band instruments typically retain better (though still limited) retrieval performance when VWC remains below 5 kg/m^2 (Kerr et al., 2010; Kim et al., 2018). In contrast, the shorter wavelength of FY-3 MWRI makes it more sensitive to vegetation structure changes, result ... [3]

Formatted: Space Before: 1 line

6:00 PM Local Solar Time, respectively, yielding a global revisit time of 2–3 days. Based on the well-validated $\tau - \omega$ radiative transfer model, this product implements both the Single Channel Algorithm using vertical polarization (SCA-V) and the Dual Channel Algorithm (DCA) for soil moisture retrieval (Chaubell et al., 2020; O'Neill et al., 2021). The characteristics of the L-band provide it with canopy penetration capabilities. Although the native spatial resolution of the radiometer is approximately 36 km, this enhanced product utilizes the Backus-Gilbert optimal interpolation technique to be distributed at a spatial sampling of 9 km on the EASE-Grid 2.0 projection.

The ASCAT retrieval data are derived from the Advanced Scatterometer onboard the MetOp-C satellite operated by the European Organization for the Exploitation of Meteorological Satellites (EUMETSAT). Following its launch in November 2018, MetOp-C has continuously provided high-quality global data, extending the long-term ASCAT data record. The satellite has equatorial crossing times of approximately 9:30 AM (descending) and 9:30 PM (ascending), providing a global revisit time of about 3 days. As an active microwave radar operating at the C-band (5.255 GHz, VV polarization), ASCAT provides global soil moisture estimates by measuring the surface radar backscatter coefficient (σ^0). This study utilizes the ASCAT Level 2 Surface Soil Moisture product (EO:EUM:DAT:METOP:SOMO12) at 12.5 km spatial sampling on the swath grid. The temporal resolution of this product relies on daily morning and evening discrete observations. Regarding the retrieval algorithm, this product is based on the TU Wien change detection algorithm, obtaining relative soil moisture, which is expressed as a degree of saturation percentage from 0 to 100%, by linearly scaling the backscatter coefficient between historical dry and wet reference lines (Bartalis et al., 2007). Subsequently, this study utilizes soil porosity data provided by the European Space Agency Climate Change Initiative (ESA-CCI) to convert this saturation into volumetric soil water content.

The MWRI soil moisture dataset was developed by the National Satellite Meteorological Center (NSMC) of the China Meteorological Administration (CMA). The FY-3D afternoon satellite was successfully launched in November 2017, with its MWRI data record officially available since early 2018. The dataset is derived from global passive microwave brightness temperature observations acquired by the MWRI instrument onboard FY-3D, which has equatorial crossing times of approximately 2:00 AM (descending orbit) and 2:00 PM (ascending orbit), providing a global revisit time of 1–2 days. Surface soil moisture is primarily retrieved from the X-band (10.65 GHz) dual-polarized brightness temperatures using a radiative transfer equation-based retrieval algorithm, in which vegetation effects are corrected and soil surface roughness effects are addressed using the Qp model (Kang et al., 2020). This daily product combines ascending and descending overpasses and is provided on a 25 km Equal-Area Scalable Earth (EASE-Grid) projection. We selected X-band retrieval products because X-band applications remain relatively limited, and we aimed to demonstrate their value through direct assimilation. Direct assimilation of radiances is certainly an important direction for land surface data assimilation. However, it requires a reasonable estimation of the errors in simulations from the radiative transfer model. This aspect warrants further investigation in future studies. The key characteristics of the three satellite soil moisture products used in this study are summarized in Table 1.

Table 1. Key characteristics of the satellite soil-moisture products used in this study.

Formatted: Font: (Asian) Times New Roman

Satellite	Band	Sampling resolution	Swath	Equatorial crossing time	Nominal revisit
SMAP radiometer	1.41 GHz	9 km	1000 km	18:00 ascending	2–3 days
MetOp-C ASCAT	5.255 GHz	12.5 km	Two 550 km swaths	21:30 ascending	3 days
FY-3D MWRI	10.65 GHz	25 km	1400 km	14:00 ascending	1–2 days

Formatted: Centered

Formatted: Centered

Formatted: Centered

Given that the spatial resolution of satellite products exceeds that of the LSM (about 1.4°×1.4°), all satellite soil moisture retrievals within each model grid cell were spatially averaged to prevent introducing excessive small-scale variability. The resulting spatially averaged soil moisture distribution is shown in Figure 1.

Deleted: ¶

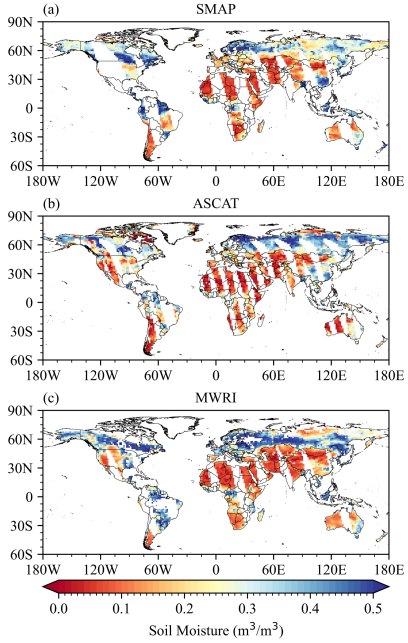


Figure 1: Spatial distribution of grid-averaged soil moisture on June 2, 2022, from (a) SMAP, (b) ASCAT, and (c) MWRI.

Before assimilation, quality control was conducted for each satellite dataset, primarily based on their native quality flags. For SMAP, we kept retrievals with quality flags of 0 or 8. For ASCAT, we retained observations with an aggregated quality flag below 50% (Chen et al., 2018). For FY3D, only observations with a quality flag of 0 were used. We then performed bias

Formatted: Space Before: 1 line

correction using cumulative distribution function (CDF) matching. Specifically, satellite-derived soil moisture was matched to the CoLM background simulations for summer 2022 and then mapped to the model's second soil layer, consistent with Albergel et al. (2017). This layer was selected because it better matches the effective sensing depth of the satellite products. In this CoLM setup, the top layer is 0–1.75 cm thick and responds quickly to rainfall, evaporation, and surface thermal forcing, so it mainly captures short-lived surface fluctuations. The second layer, which spans 1.75–4.51 cm, is closer to the main sensing depth of SMAP and ASCAT (about 0–5 cm) and provides a more stable representation of near-surface soil moisture. It was therefore used for observation mapping and bias correction.

2.2 In-Situ Data

In-situ data were selected to validate the assimilation results. Soil moisture and precipitation observations were obtained from the ISMN and the CMA station network. The ISMN comprises over 1,400 stations across 35 international networks (Dorigo et al., 2021). The CMA network maintains an extensive infrastructure of surface meteorological stations across China. To ensure data reliability, quality control was performed based on the original quality flags provided by each network prior to validation, retaining only valid measurements. For the ISMN dataset, which includes the USCRN, COSMOS-UK, SOILSCAPE, ARM, TAHMO, SMOSMANIA, and FR_Aqui networks, we utilized the station-specific quality flags and only kept observations marked as 'G'. Similarly, only valid observations with a quality flag of 0 were retained for the CMA network. To maximize the spatial coverage for evaluation, this study did not impose a strict threshold on time-series completeness during the quality control process, ensuring that all valid observations passing the physical screening were included in the analysis.

A total of 3057 stations remained after these quality control procedures. Figure 2 illustrates the spatial distribution of the CMA and ISMN in-situ stations to provide a clear visualization of the ground-based data coverage. Among these, 2792 CMA stations are densely distributed across most of China as shown in Figure 2a. Additionally, a total of 265 ISMN stations were utilized, with the majority located in the United States and others distributed across Europe and Africa. Given that the highest station density occurs in the U.S. region, Figure 2b primarily highlights the distribution of ISMN stations in that area.

In this study, the 10 cm soil depth was used for primary validation to bridge the gap between satellite sensing and in-situ monitoring. Since L-, C-, and X-band microwave observations mainly reflect near-surface soil moisture, and 10 cm is the shallowest standardized measurement depth also has the fewest missing values across the CMA station network. To better align with the research objectives and ensure a sufficient number of validation data points, we focus on evaluating the impact of land data assimilation on 10 cm soil moisture.

Formatted: Space Before: 1 line

Formatted: English (US)

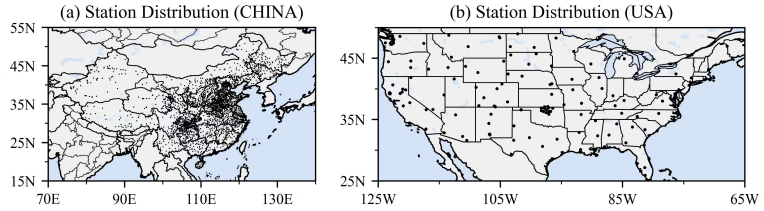


Figure 2: Spatial distribution of the in-situ soil moisture stations. (a) China Meteorological Administration network, and (b) International Soil Moisture Network stations located in the United States.

2.3 ERA5-Land Reanalysis Data

To improve the global applicability of validation, this study incorporates the ERA5-Land dataset developed by the European Centre for Medium-Range Weather Forecasts (ECMWF) under the Copernicus Climate Change Service (C3S) (Muñoz-Sabater, 2019). ERA5-Land is a high-resolution enhancement of the ERA5 reanalysis, focusing on land surface variables. Its soil moisture product includes four layers (0–7 cm, 7–28 cm, 28–100 cm, and 100–289 cm) providing volumetric water content.

Formatted: Space Before: 1 line

3 Model and Experimental Design

3.1 CoLM model

This study uses the CoLM to simulate land surface processes. Developed primarily by Chinese research institutions, CoLM originated from integrating the IAP94 and CLM frameworks through collaboration between the Institute of Atmospheric Physics, Chinese Academy of Sciences, and NCAR. The model represents coupled soil hydrothermal and vegetation ecophysiological processes, and is widely applied in Earth system studies. We use the 2014 version, which incorporates major advances in soil physics and vegetation parameterizations, including an updated soil hydraulic scheme and a two-big-leaf canopy model. The model consists of 10 vertically stratified soil layers from the surface to bedrock. Specifically, the bottom depths of these 10 layers are 1.75, 4.51, 9.06, 16.55, 28.91, 49.29, 82.89, 138.28, 229.61, and 380.19 cm, respectively. Soil moisture is simulated by numerically solving the Richards equation, accounting for root uptake, infiltration, and surface and subsurface runoff. Vegetation processes follow a plant functional type (PFT) approach, with a two-big-leaf scheme separating sunlit and shaded leaves to better represent canopy radiative and energy transfer (Dai et al., 2003; Li et al., 2017). In this study, the Leaf Area Index (LAI) is prescribed from the monthly reprocessed MODIS LAI dataset, which was generated following the approach of Yuan et al. (2011). This prescribed LAI drives the two-big-leaf canopy scheme in CoLM to partition the canopy into sunlit and shaded leaves and to compute canopy-scale radiation absorption, photosynthesis, stomatal conductance, and transpiration. Hydrological processes include precipitation interception, infiltration, evapotranspiration, and runoff generation, with subgrid-scale heterogeneity in topography, soil, and vegetation types explicitly considered. For the

Formatted: Space Before: 1 line

simulations conducted in this study, the model is configured with a horizontal spatial resolution of 1.4°×1.4° and an output temporal resolution of 1 hour.

3.2. CoLM Atmospheric Forcing

The atmospheric forcing data are derived from the ERA5 near-surface atmospheric variables, including downward shortwave and longwave radiation, precipitation, air pressure, specific humidity, air temperature, and wind speed (Hersbach et al., 2020). A bilinear interpolation method was used to interpolate the ERA5 data from its original 0.25° horizontal resolution to a 1.4°grid. The interpolated forcing data have a temporal resolution of 3 hours and cover the period from January 1, 1979, to December 31, 2022. For the model integration, the CoLM employs an explicit finite-difference method with a time step of 30 minutes to ensure simulation stability and accuracy. The model outputs, including soil temperature, moisture, surface fluxes, evapotranspiration, and runoff, provide a foundation for subsequent data assimilation and evaluation.

3.3. SEKF assimilation system

To accommodate the strong nonlinearities characteristic of land-surface processes, the Simplified Extended Kalman Filter (SEKF)—an assimilation scheme that dispenses with the adjoint model—is employed herein for soil-moisture data assimilation. SEKF was proposed by Hess (2001) and Balsamo et al. (2004) based on the Extended Kalman Filter (EKF). It approximates the derivative of the nonlinear observation operator by adding appropriate perturbations, thereby avoiding the development of a cumbersome adjoint model. Compared to the EKF, SEKF does not require local linearization of model equations and updates the observation operator gradient in real time, thereby retaining some flow-dependent error characteristics. The method is computationally efficient and has been implemented in land data assimilation systems such as that of ECMWF (Drusch et al., 2009; de Rosnay et al., 2013; Herbert et al., 2024).

The analysis update step of the SEKF is consistent with the Kalman filter. First, the state is updated by weighting the difference between the observation and the simulated observation (i.e., Observation-Minus-Background, OMB) with the Kalman gain matrix **K**:

$$\boldsymbol{x}^{\mathrm{a}} = \boldsymbol{x}^{\mathrm{b}} + \mathbf{K}\left[\boldsymbol{y} - \boldsymbol{\mathcal{H}}\left(\boldsymbol{x}^{\mathrm{b}}\right)\right] \quad (1)$$

Here, $\boldsymbol{x}^{\mathrm{a}}$ is the analysis state, $\boldsymbol{x}^{\mathrm{b}}$ is the background state, $\boldsymbol{y}$ is the observation, and $\boldsymbol{\mathcal{H}}$ is the nonlinear observation operator. The Kalman gain matrix **K** is computed as follows:

$$\mathbf{K} = \mathbf{B}\mathbf{H}^{\mathrm{T}}\left(\mathbf{H}\mathbf{B}\mathbf{H}^{\mathrm{T}} + \mathbf{R}\right)^{-1} \quad (2)$$

B is the background error covariance, **R** is the observation error covariance, and **H** is the linearized observation operator. To account for the nonlinear nature of the observation operator in LSM, the SEKF computes **H** using a finite-difference perturbation approach. Specifically, a small perturbation $\delta\mathbf{x}_j$ is applied to each component $\mathbf{x}_i$ of the state vector, and the

Formatted: Space Before: 1 line

Formatted: Space Before: 1 line

Formatted: English (US)

Formatted: Space Before: 1 line

Formatted: Space Before: 1 line

resulting change in the simulated observation is used to approximate the first-order derivative of the observation operator with respect to that state component:

$$\mathbf{H}_{ij} = \frac{\mathcal{H}(\mathbf{x}_i+\delta\mathbf{x}_i)-\mathcal{H}(\mathbf{x}_i)}{\delta\mathbf{x}_j} \quad (3)$$

The observation operator is estimated using the finite-difference approach described above. Each perturbation must be small enough to satisfy the linear approximation yet large enough to avoid numerical noise. According to the limit definition of the derivative, the derivative of a function can be approximated via the finite difference method. For any given model grid point, the first-order derivative of the observation operator can thus be calculated by introducing a small perturbation to the independent variable. As the perturbation amplitude becomes sufficiently small, the difference between the perturbed and unperturbed function values of the observation operator approximates its first-order derivative. To identify a sufficiently small perturbation, the right derivative $\mathbf{H}^+$ and left derivative $\mathbf{H}^-$ are evaluated and compared. When the discrepancy between $\mathbf{H}^+$ and $\mathbf{H}^-$ approaches zero, their mean value is adopted as the first-order derivative of the observation operator at the corresponding grid point (Balsamo et al., 2007). To minimize the influence of meteorological variability, we calculated globally averaged derivatives over all grid points under different perturbation magnitudes (Figure 3). As an example, for the second soil layer (Figure 3b), a perturbation of 10^{-3} m^3/m^3 produced a stable derivative of approximately 0.35, while the difference between $\mathbf{H}^+$ and $\mathbf{H}^-$ is close to zero. Based on this criterion, the optimal perturbation values for the first seven soil layers are selected as 0.001, 0.0001, 0.0001, 0.0001, 0.0005, 0.001, and 0.0005 m^3/m^3, respectively.

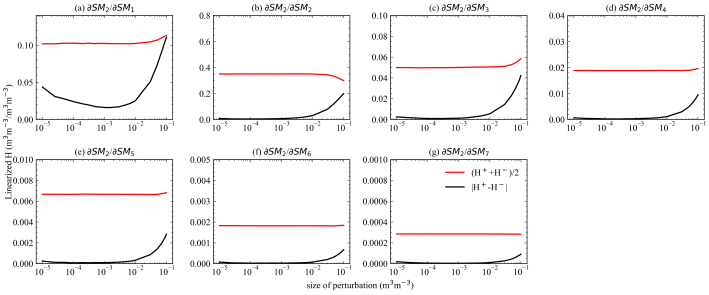


Figure 3: The $\partial SM_2/\partial SM_n$ characteristics with respect to size of perturbation in different layers are shown. The black line represents $|\mathbf{H}^+-\mathbf{H}^-|$, and the red line represents $(\mathbf{H}^+ + \mathbf{H}^-)/2$.

The configuration of background and observation errors in this study follows the methodology established by Bai et al. (2025). For areas without station observations, errors are characterized by the root-mean-square error (RMSE) against the ERA5-Land product. In station-covered regions, observation and background errors are estimated via TC using CoLM simulations, in-situ data, and satellite retrievals as independent inputs. These TC estimates were scaled to match RMSE magnitudes to ensure consistency. Spatial patterns of these errors are shown in Figure 4. Based on these estimated errors, and following de Rosnay

Formatted: Space Before: 1 line

Formatted: Space Before: 1 line

et al. (2013), we specified both the background and observation error covariance matrices as diagonal, with their diagonal entries derived from the errors. In the assimilation process, only land pixels are considered according to CoLM's underlying surface data, while inland water and frozen soil grids are masked. Additionally, a 3-sigma innovation check is applied, rejecting any observations that deviate from the background by more than three standard deviations.

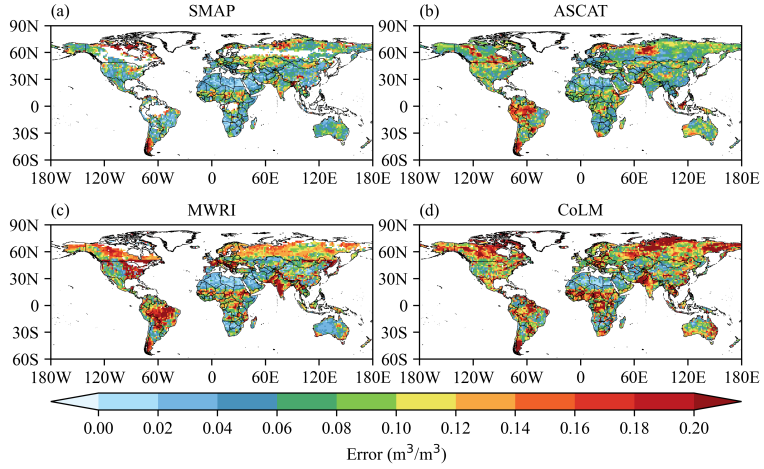


Figure 4: Spatial distributions of observation and background errors for different satellites. (a) SMAP observation error; (b) ASCAT observation error; (c) MWRI observation error; and (d) CoLM background error.

3.4. Experiment design

The primary objective of this study is to quantify the extent to which assimilating diverse soil-moisture retrievals can enhance the skill of the CoLM in simulating the land surface variables. To ensure the deep-layer soil variables reached a statistical equilibrium, the model was first spun up for 342 years from a cold start. This spin-up was run entirely in open loop, with all assimilation experiments starting from the same open-loop initial conditions rather than from a separate assimilation spin-up. Subsequently, a series of sensitivity experiments were designed to quantify the assimilation efficacy of different soil moisture products.

Three groups of numerical experiments were conducted. The first is a control experiment (CTL), serving as a reference benchmark. In CTL, the CoLM was integrated from a hot start for two months (2 June–1 August 2022) without data assimilation. In the second experiment suite, the SEKF assimilation module is activated to sequentially ingest SMAP-, ASCAT-, and MWRI-derived soil-moisture products, designated as the DA_L, DA_C, and DA_X experiments, respectively.

Formatted: Space Before: 1 line

Each experiment consists of one month of daily assimilation cycles, followed by a one-month free forecast. Observations were assimilated once daily at 0000 UTC. The third group of experiments was conducted to investigate the effects of continuous data assimilation on model performance in simulating the soil moisture. This set involved continuous assimilation over the entire two-month study period, encompassing the assimilation of single datasets (DA_L, DA_C, and DA_X), their pairwise combinations (DA_L+C, DA_L+X, DA_C+X), and all three datasets simultaneously (DA_ALL). A summary of all experiment configurations is provided in Table 2.

Deleted: 1

Deleted: 1

Table 2. Experiment design.

Group	Experiment	Assimilated product(s)	Assimilation phase	Forecast phase
One	CTL			20220602-20220801
Two	DA_L	SMAP	20220602-20220703	20220703-20220801
	DA_C	ASCAT	As above	As above
	DA_X	MWRI	As above	As above
Three	DA_L	SMAP	20220602-20220801	
	DA_C	ASCAT	As above	
	DA_X	MWRI	As above	
	DA_L+C	SMAP+ASCAT	As above	
	DA_L+X	SMAP+MWRI	As above	
	DA_C+X	ASCAT+MWRI	As above	
	DA_ALL	SMAP+ASCAT+MWRI	As above	

A once-daily assimilation cycle was used in this study. Soil moisture has clear temporal persistence, and its day-to-day variability can therefore be adequately represented at a daily update interval. This choice is also consistent with the temporal characteristics of the input products, since ASCAT and SMAP are instantaneous satellite retrievals, whereas the FY-3D MWRI product used here is a fused daily product without a specific observation time. Using a 24 h assimilation window thus provides a common framework for integrating the three datasets. In addition, a higher update frequency would markedly increase the computational burden of the SEKF, which requires perturbation integrations to estimate the Jacobian of the observation operator at each analysis step. Furthermore, this daily approximation has negligible impact on the results. As shown in Figure S1, the global mean diurnal variation in soil moisture is about 0.0006 m^3/m^3, much smaller than the typical satellite retrieval uncertainty of about 0.04 m^3/m^3. This approximation is therefore adequate for the temporal scale of this study and has little effect on the global soil moisture estimates.

Formatted: Space Before: 1 line

3.5 Evaluation Metrics

To quantitatively evaluate the differences among various assimilation experiments, the correlation coefficient, RMSE, and unbiased RMSE (ubRMSE) were selected as the primary evaluation metrics in this study. The specific formulas are defined as follows:

$$R = \frac{\sum_{i=1}^{N}(x_i - \bar{x})(y_i - \bar{y})}{\sqrt{\sum_{i=1}^{N}(x_i - \bar{x})^2}\sqrt{\sum_{i=1}^{N}(y_i - \bar{y})^2}} \quad (4)$$

$$\mathrm{RMSE} = \sqrt{\frac{1}{N}\sum_{i=1}^{N}(x_i - y_i)^2} \quad (5)$$

$$ubRMSE = \sqrt{\frac{1}{N}\sum_{i=1}^{N}[(x_i - \bar{x}) - (y_i - \bar{y})]^2} \quad (6)$$

where x_i and y_i denote the evaluated assimilation data and the reference data at the i-th sample, respectively; $\bar{x}$ and $\bar{y}$ represent their respective sample means; and N is the total number of samples involved in the statistics. The correlation coefficient is used to characterize the consistency between the two datasets in spatial distribution or temporal variation, RMSE is used to measure the overall error, and ubRMSE is used to represent the error after removing the systematic bias.

4. Results

4.1. Comparison of Assimilation Performance for Different Frequency Bands

Comparing Group 1 (CTL) and Group 2 (assimilation experiments) clarifies the forecast improvements from land data assimilation. ERA5-Land soil moisture is used to quantify the effect of assimilating L-, C-, and X-band satellite retrievals on the simulations. Figure 5 shows spatial correlation coefficients (R) and root-mean-square error (RMSE) relative ERA5-Land. For each soil layer and each time step, R and RMSE were calculated over all available global land grid cells, with ERA5-Land as the reference. Assimilation from all three bands improves soil moisture accuracy across 0–1 m, with band- and depth-dependent magnitudes. C-band yields the largest gains, R increases by 0.15, 0.12, and 0.09 and RMSE decreases by 0.020, 0.015, and 0.012 m^3/m^3 for the 0–7 cm, 7–28 cm, and 30–100 cm layers, respectively. L-band ranks second in performance and exhibits clear depth-dependent variations. At the surface layer, its ΔR reaches 0.13, which exceeds that of X-band (0.11). In the second layer, the improvements are comparable between the two, while in the third layer, L-band performs slightly worse than X-band. In the forecast phase, the results differ from those in the assimilation phase. L-band shows the smallest improvement in both R and RMSE, suggesting a more rapid loss of its assimilation impact. In contrast, the effects of C- and X-band assimilation remain more persistent throughout the forecast period. It should be noted that ERA5-Land is an offline simulation driven by ERA5 atmospheric forcing. Because ERA5 itself has already assimilated ASCAT soil moisture data, this indirect coupling implies that the validation process is not strictly independent. This relationship might lead to an overestimation of the skill scores for ASCAT to some degree.

Formatted: Font: (Asian) Times New Roman
Formatted: Space Before: 1 line
Formatted: Space Before: 1 line
Formatted: Font: (Asian) Times New Roman
Formatted: Space Before: 1 line

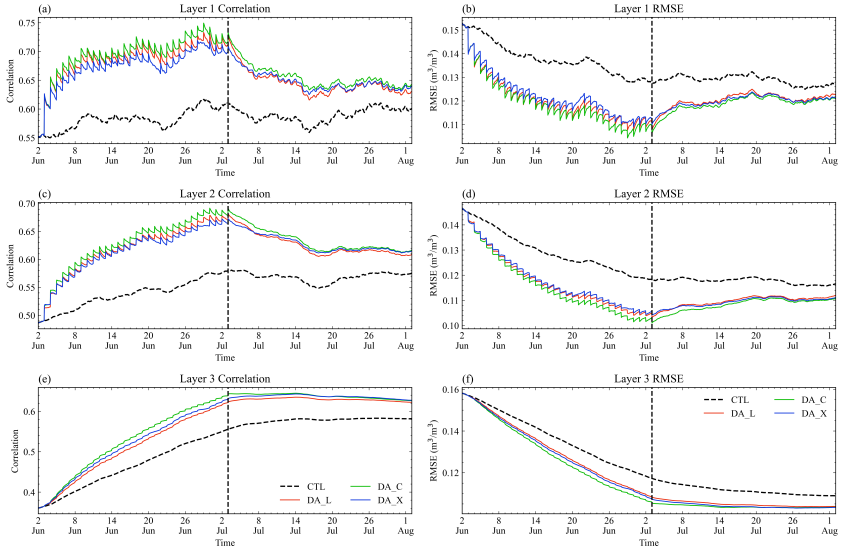


Figure 5: Spatial correlation coefficients (left panels) and RMSE (right panels) of soil moisture relative to ERA5-Land for different experiments. (a, c, e) is spatial correlation coefficients for layer 1, layer 2, and layer 3, respectively, and (b, d, f) is the corresponding RMSE for layer 1, layer 2, and layer 3, respectively. The region to the left of the vertical dashed line denotes the assimilation phase, and the region to the right denotes the forecast phase. The dashed line represents the CTL, while red, green, and purple lines represent the assimilation of L-, C-, and X-band soil moisture products, respectively.

To further explore the causes of performance differences among the frequency bands, the mean first-layer soil moisture is analyzed. Since microwave signals at different frequencies are affected differently by vegetation, the vegetation distribution is also considered in the analysis. The vegetation type data used in this study are derived from the built-in dataset of the CoLM. Considering that each model grid cell typically contains multiple vegetation types, we select the vegetation type with the largest area fraction within each grid cell as the representative vegetation type. As shown in Figure 6, the analysis fields exhibit notable spatial variations and a clear latitudinal dependence. Over southeastern China between 10°–30°N, which is predominantly covered by forest vegetation, all three experiments identify the region as having high soil moisture, yet the DA_L experiment is comparatively wetter and in closer agreement with ERA5-Land. At higher latitudes, such as northern Canada and Siberia, the dry–wet contrast is more pronounced in the DA_X and DA_C experiments. However, theDA_L experiment exhibits an overly dry bias that deviates from ERA5-Land. In the wetter regions of southeastern Australia, which are mainly dominated by grass vegetation, the X-band results most closely match ERA5-Land, while the DA_C experiment displays a distinct dry bias. These results indicate that the assimilation performance of different frequency bands exhibits strong regional dependence.

Formatted: Space Before: 1 line

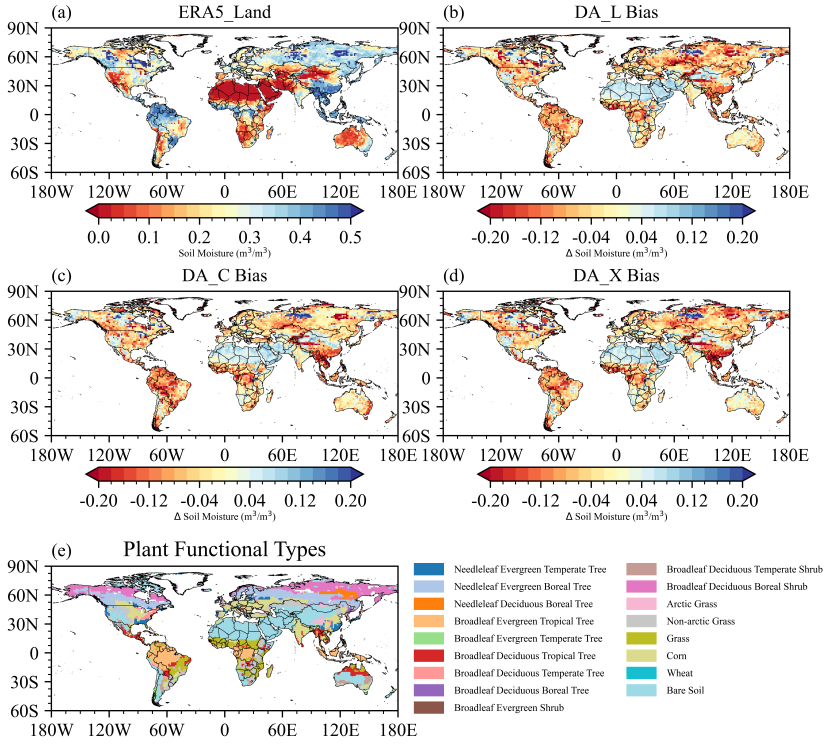


Figure 6: Spatial distribution of mean soil moisture in the top layer (0-7 cm) during 2 June to 3 July 2022. (a) shows the soil moisture from the ERA5_Land product. (b)–(d) show the soil moisture differences of the analysis fields from the DA_L, DA_C, and DA_X assimilation experiments relative to ERA5_Land, respectively (i.e., DA experiment minus ERA5-Land). (e) shows the spatial distribution of vegetation cover.

To further clarify the regional dependence of assimilation performance, the global land surface was divided into three latitudinal bands: 90°S–30°S, 30°S–30°N, and 30°N–90°N. Spatial correlation coefficients and RMSE were computed for each zone, as shown in Figure 7. The calculation follows the same method as the global analysis, but is applied separately within each latitudinal band, and the resulting time-step metrics are averaged over the corresponding period. In the CTL, the best model performance can be found in the tropics (30°S–30°N), where spatial correlation reached 0.8 and RMSE was approximately 0.115 m^3/m^3. In contrast, performance was poorest in the Northern Hemisphere (30°N–90°N), with correlation around 0.4 and RMSE exceeding 0.15 m^3/m^3.

Formatted: Space Before: 1 line

Assimilation experiments show that in the Southern Hemisphere and tropical regions, the L-band provides the most notable improvement during both the assimilation and forecast phases. For example, in the 90°S–30°S band, the second-layer soil moisture correlation increased by 0.10 and RMSE decreased by 0.015 m^3/m^3. However, in the Northern Hemisphere (30°N–90°N), the DA_C and DA_X experiments outperformed DA_L. In particular, C-band assimilation improved the second-layer correlation by 0.16 and reduced RMSE by 0.024 m^3/m^3 relative to the CTL, indicating the best performance in this region.

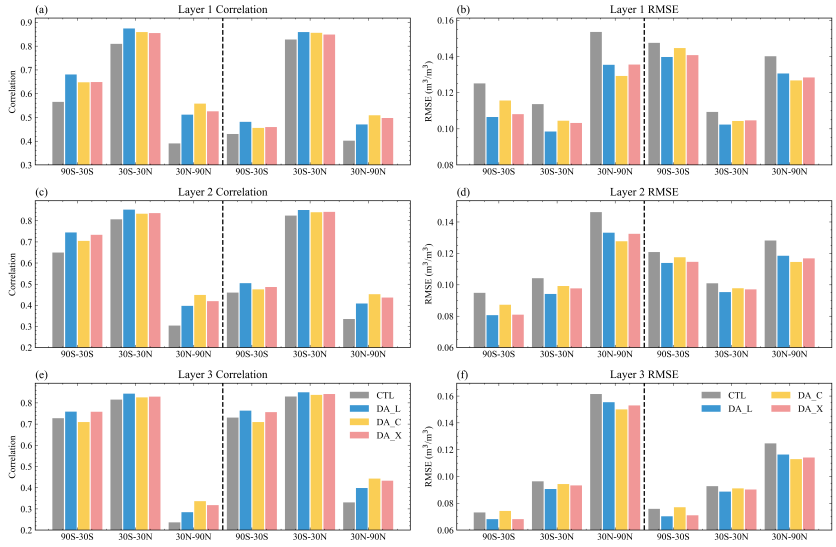


Figure 7: Spatial correlation coefficients (left panels) and RMSE (right panels) of soil moisture relative to ERA5-Land across different latitudinal zones for the four experiments. (a, c, e) is spatial correlation coefficients for layer 1, layer 2, and layer 3, respectively, and (b, d, f) is the corresponding RMSE for layer 1, layer 2, and layer 3, respectively. The left and right sides of the vertical dashed line correspond to the assimilation and forecast phases, respectively. Gray represents the control experiment, while blue, yellow, and pink represent assimilation of SMAP, ASCAT, and FY-3D soil moisture products, respectively.

Given the differing penetration capabilities of microwave frequencies and the strong correlation between vegetation density and latitude, variations in vegetation type likely contribute to the observed latitudinal differences in assimilation performance. Figure 8 shows the evaluation results of the assimilation experiments across different vegetation types, validated against ERA5-Land to ensure sufficient sample sizes. The vegetation types are sorted in ascending order based on the average precipitation of each region during the assimilation period. For clarity, a comprehensive list of vegetation abbreviations has been provided in Table 3. The calculation follows the same method as the latitudinal-band analysis, but is applied separately to land grid cells belonging to each representative vegetation type. Assimilation of MWRI X-band data performs best in

Deleted: ¶

sparsely vegetated regions, with consistent improvements across all soil depths. In contrast, in densely vegetated areas, the deeper penetration of lower-frequency sensors becomes evident. SMAP (L-band) demonstrates the most stable performance, particularly in deeper soil layers. For example, in temperate broadleaf forests (BET Temperate), the improvement in correlation for deep-layer soil moisture exceeds that of the surface layer, while the DA_X experiment exhibits a negative impact. These results align with findings from Mousa and Shu (2020), who used the TC method and reported that SMAP significantly outperformed ASCAT in forested regions of Africa.

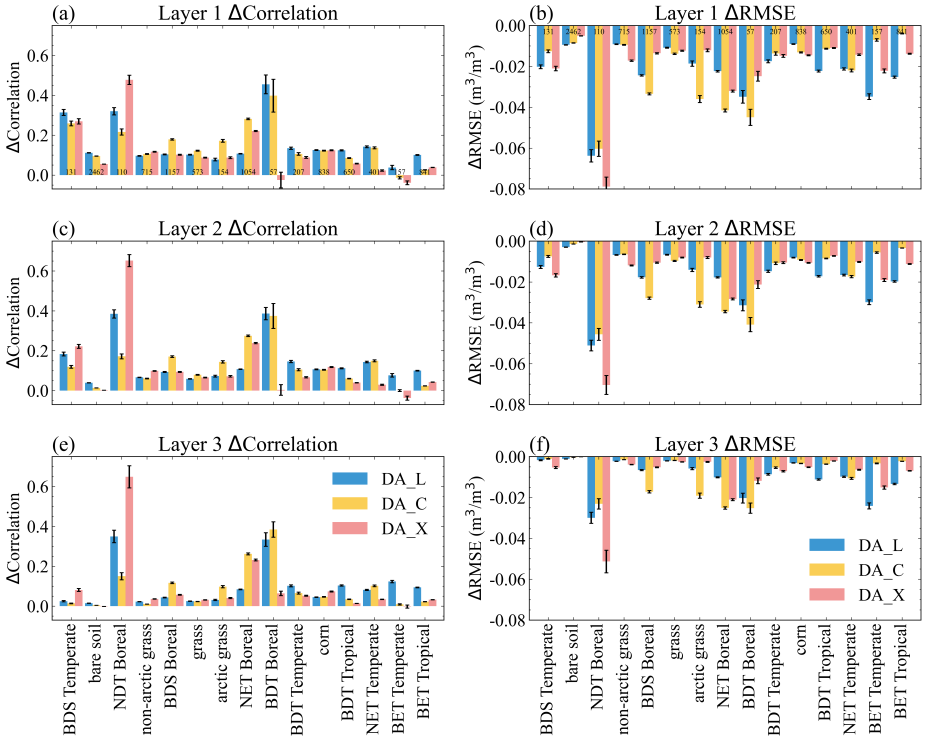


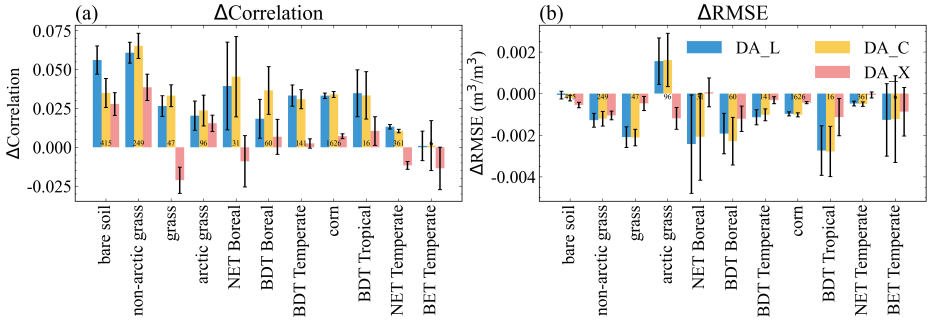
Figure 8: Changes in correlation coefficient (left panels; after-minus-before assimilation) and RMSE (right panels; after-minus-before assimilation) of soil moisture relative to ERA5-Land during 2 June to 3 July 2022, shown as a function of vegetation type. (a, c, e) is correlation coefficients for layer 1, layer 2, and layer 3, respectively, and (b, d, f) is the corresponding RMSE for layer 1, layer 2, and layer 3, respectively. Error bars denote 95% confidence intervals, and numbers below represent the sample size, which is identical across all groups.

Table 3 Vegetation types.

Deleted: 2

Abbreviation	Type
BDS Temperate	Broadleaf deciduous temperate shrub
NDT Boreal	Needleleaf deciduous boreal tree
BDS Boreal	Broadleaf deciduous boreal shrub
NET Boreal	Needleleaf evergreen boreal tree
BDT Boreal	Broadleaf deciduous boreal tree
BDT Temperate	Broadleaf deciduous temperate tree
BDT Tropical	Broadleaf deciduous tropical tree
NET Temperate	Needleleaf evergreen temperate tree
BET Temperate	Broadleaf evergreen temperate tree
BET Tropical	Broadleaf evergreen tropical tree

Recognizing that reanalysis data are not absolute truth, we further evaluated the assimilation performance using in situ observations from ISMN and CMA. Figure 9 presents correlation and RMSE statistics for each experiment. The vegetation types follow the same order as in Figure 8. For each station, the correlation coefficient and RMSE are calculated from the time series of simulated and observed soil moisture during the assimilation period, and the results are then grouped by vegetation type. Some vegetation types are omitted due to a lack of corresponding station data. The correlation results show that both L-band and C-band assimilation consistently improve model performance across all available vegetation types, except in the Arctic Grass region where RMSE increases slightly. Notably, in densely vegetated areas, assimilation of the MWRI product leads to a decline in correlation, highlighting its limited effectiveness under dense canopy conditions. These findings are consistent with the reanalysis-based evaluation and reinforce the robustness of the earlier conclusions.



Formatted: Space Before: 1 line

Figure 9: Same as Figure 5, but for comparison between model soil moisture and in situ observations at 0–10 cm depth. (a) is correlation coefficients for 0-l0 cm, and (b) is the corresponding RMSE for 0-10 cm. Error bars denote 95% confidence intervals, and numbers below represent the sample size, which is identical across all groups.

As defined in the experimental design, the primary difference among the experiments lies in the observation data used. Given that all satellite products achieve near-global coverage during the one-month continuous assimilation period, differences in assimilation performance are largely attributed to observation errors. To explore the relationship between assimilation performance and vegetation type, we evaluated the retrieval accuracy of each satellite product using in situ soil moisture observations under different vegetation types. Figure 10 presents the correlation and RMSE of SMAP, ASCAT, and MWRI retrievals against in situ measurements, with vegetation types ordered as in Figure 8.

The retrieval accuracy of all three products exhibits a clear dependence on vegetation density. Owing to the stronger canopy penetration capability of L-band microwave radiometry, SMAP maintains relatively higher correlation and lower RMSE in densely vegetated areas compared to the other products. ASCAT exhibits competitive overall performance relative to SMAP, owing partly to its robust time-series change detection algorithm. It tends to slightly outperform SMAP in low- and sparse-vegetation regions but performs marginally worse in moderate-to-high vegetation zones due to greater C-band signal attenuation. In contrast, the X-band MWRI product is notably inferior to both SMAP and ASCAT in moderately and densely vegetated areas owing to its shorter wavelength and limited penetration. Over sparsely vegetated and bare-soil regions, however, MWRI achieves accuracy that is comparable, or occasionally marginally superior, to the other two products. These results suggest that spatial variations in assimilation performance are primarily driven by the intrinsic differences in retrieval accuracy among the products. In summary, the relatively longer wavelengths of the L-band and C-band, combined with robust retrieval algorithms, enable SMAP and ASCAT to maintain high accuracy in vegetated areas, while the shorter X-band (MWRI) is more severely limited by vegetation-induced scattering and attenuation.

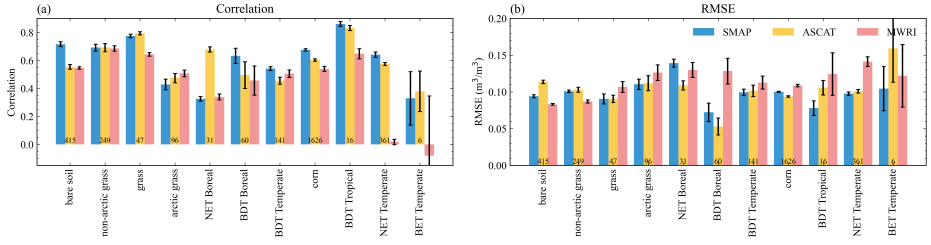


Figure 10: Correlation coefficients (a) and RMSE (b) between satellite-retrieved soil moisture and in situ observations. Light blue, orange, and red bars represent SMAP, ASCAT, and MWRI products, respectively. Error bars denote 95% confidence intervals, and numbers below represent the sample size, which is identical across all groups.

Formatted: Space Before: 1 line

The vegetation-dependent differences in assimilation performance may help explain the pattern observed in Figure 5, where the impact of L-band assimilation decays more rapidly during the forecast phase. Figure 11 illustrates the impact of precipitation on the persistence of assimilation increments. Figure 11a uses a typical BET Tropical grid point (6.38°N, 59.06°W) as an example to present the soil moisture time series. During the assimilation phase, continuous observational constraints result in a distinct divergence between the soil moisture sequences of the Data Assimilation (DA) experiment and the Control (CTL) experiment. However, in the forecast phase, external forcings such as heavy precipitation dominate the soil moisture state. This causes the DA and CTL simulation results to rapidly converge, which makes the information introduced via assimilation more susceptible to being masked. Figure 11b further demonstrates that densely vegetated regions, including BET Tropical and NET Temperate, typically experience higher average precipitation. Because L-band assimilation performs relatively well in these regions, frequent and intense precipitation may partly explain the more rapid decay of its impact during the forecast phase. In contrast, based on the statistical results, the assimilation of C band and X band products led to improvements in assimilation performance in regions with low to moderate vegetation cover. In these areas, less frequent precipitation and slower soil moisture dynamics allow the assimilated signal to persist longer, resulting in better forecast retention.

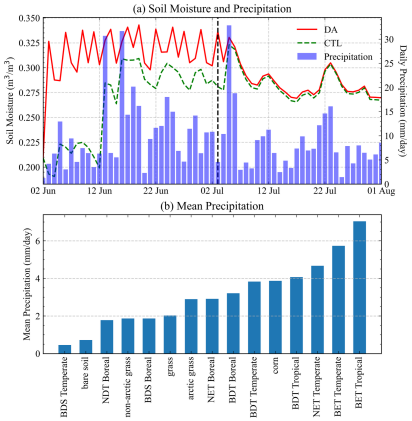


Figure 11: (a) Time series of daily precipitation and simulated soil moisture from the data assimilation (DA) and CTL experiments at a representative BET Tropical grid cell (6.38°N, 59.06°W). The vertical dashed line separates the assimilation phase and the forecast phase. (b) Mean precipitation across different vegetation types during the study period.

Formatted: Space Before: 1 line, Widow/Orphan control

Deleted: Consequently, in these regions where the assimilation of L-band retrieval products otherwise performs relatively well, frequent and intense precipitation acts as an external forcing that quickly obscures the initial assimilation information, resulting in a more rapid decay in forecast skill. While L-band performs best in regions with dense vegetation and high precipitation (Mousa and Shu, 2020), soil moisture in these areas is frequently influenced by strong meteorological forcings such as rainfall. As a result, the assimilated information is more likely to be masked by subsequent hydrometeorological variability, leading to faster loss of forecast skill.

Deleted: However, it should be emphasized that such assimilation systems improve background field accuracy from a probabilistic perspective, which does not necessarily imply that the original satellite retrieval products themselves possess high precision. For active microwave sensors such as ASCAT, the penetration depth of radar signals increases significantly under extremely dry soil conditions, which triggers subsurface volume scattering effects and impacts the data quality of the soil moisture retrieval products (Wagner et al., 2013).

4.2. Synergistic Assimilation Performance Analysis

4.2.1. Complementarity of Multi-band Soil Moisture Products

Formatted: Heading 3

Formatted: Space Before: 1 line

The preceding analyses demonstrate marked disparities in the assimilation efficacy of individual satellite products, underscoring the imperative of simultaneous multi-satellite data assimilation. To quantify the incremental benefit of assimilating various satellite-data combinations, Figure 12 displays the probability density functions (PDFs) of the differences between the spatial correlation coefficients of soil-moisture analyses from each assimilation experiment and those from the control experiment, with correlations calculated against in-situ observations. All PDFs exhibit a pronounced positive skew, indicating that every assimilation experiment outperforms the control. Moreover, dual-satellite assimilation systematically surpasses single-satellite assimilation, corroborating the added value of synergistic multi-source data integration for enhanced assimilation efficacy. Among the combinations, the DA_L+C experiment shows the best performance. This improvement is likely due to the complementary characteristics of L- and C-band sensors under varying vegetation conditions: Due to its longer wavelength, the L band possesses a relatively stronger penetration capability through the vegetation canopy. Consequently, in regions with denser vegetation cover, the assimilation of L band products demonstrates relatively better performance than the assimilation of C band and X band products. However, in regions with extremely high vegetation cover, such as dense forests, the thickness of the canopy and the high-water content within the vegetation absorb and scatter microwave signals, resulting in a decline in the quality of all soil moisture retrieval products. And C-band is more effective in low-to-moderate vegetation environments. Together, they provide more balanced and robust performance across diverse land surface conditions. This is consistent with the findings of Kim et al. (2018), who employed a method based on maximizing the correlation coefficient to merge different soil moisture products. Their results indicated that SMAP exhibited broader compatibility with products from other frequency bands. Notably, in densely vegetated regions, the combination of SMAP and ASCAT outperformed other fusion schemes. However, assimilating all three satellite products does not further improve performance over the SMAP and ASCAT combination and, in some cases, leads to degradation. For example, the probability density function of performance metrics shows more frequent negative values in the DA_ALL case compared to DA_L+C. This suggests that the inclusion of lower-quality data can reduce overall assimilation effectiveness in multi-source systems.

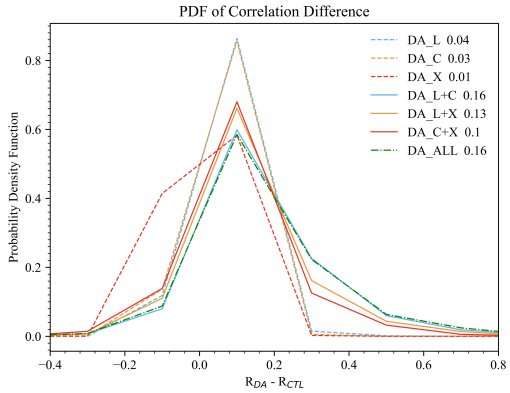


Figure 12: Probability density distributions of the correlation coefficient differences between assimilation experiments and the CTL, based on in situ observations. Legend values indicate the mean correlation improvement for each experiment.

To explain the negative impact observed when adding MWRI data to the SMAP and ASCAT combination, we analyzed a subset of representative vegetation types, Temperate Needleleaf Forest (NET Temperate), non-Arctic grassland, and corn. Figure 13 shows the changes in correlation and RMSE when a third satellite product is added to a two-source combination for each vegetation type. Adding SMAP (L-band) to the ASCAT and MWRI combination led to consistent improvements across all three vegetation types, with increases in correlation and reductions in RMSE. This effect was most pronounced in non-Arctic grasslands, where correlation improved by 0.09 and RMSE decreased by 0.0015 m^3/m^3. Adding ASCAT (C-band) to the SMAP and ASCAT combination also improved performance, though to a lesser extent. In contrast, incorporating MWRI (X-band) into the SMAP and ASCAT combination produced minimal benefit and even reduced the correlation in the densely vegetated NET Temperate region.

Formatted: Space Before: 1 line

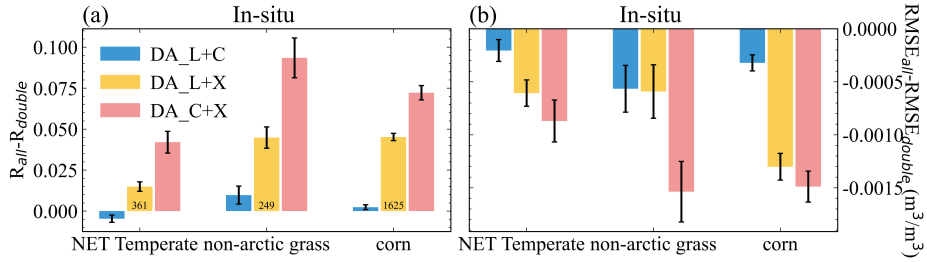
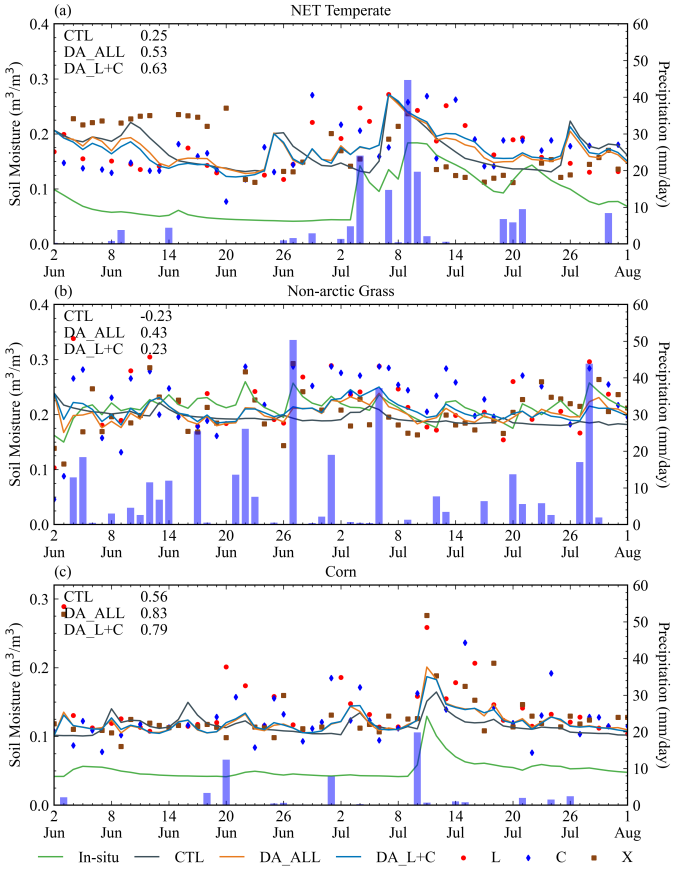


Figure 13: Changes in correlation coefficient (a) and RMSE (b) between model output and in situ observations after adding a third satellite product to each two-product assimilation combination, shown for selected vegetation types. Error bars denote 95% confidence intervals, and numbers below represent the sample size, which is identical across all groups. The label "all" denotes the simultaneous assimilation of L-band, C-band, and X-band data, while "double" refers to the assimilation of only two of them, which can be either L and C, L and X, or C and X.

To better understand how vegetation influences the assimilation performance of different satellite products, a time-series validation was conducted using in situ observations. To ensure objectivity and representativeness, three stations were randomly selected from different representative land cover types: NET Temperate (-83.39°, 33.78°), non-Arctic grassland (105.23°, 37.40°), and Corn (121.06°, 42.39°). Figure 14 presents daily mean soil moisture from model simulations across different assimilation experiments, along with satellite retrievals and station observations. Consistent with the spatially averaged results, for the station in NET Temperate area (Figure 14a). The time-series correlation for DA_ALL (0.53) was lower than that of DA_L+C (0.63). As can be seen, during June 2–20, the soil moisture from MWRI (brown squares) is notably higher than that of the other two products and in situ observations. This results in the soil moisture analysis from the DA_ALL experiment being significantly higher than that from DA_L+C, which clearly demonstrates that erroneous information in the MWRI product degrades the final assimilation performance.

In contrast, for the Corn vegetation type (Figure 14c), the DA_ALL experiment showed the highest accuracy, achieving a correlation of 0.83 with station data, compared to 0.56 for the CTL and 0.79 for the DA_L+C experiment. The inclusion of MWRI (X-band) data improved the model's ability to capture soil moisture responses to rainfall events, especially when SMAP (L-band) and ASCAT (C-band) data were unavailable on certain days (e.g., July 12). During the mid-July precipitation event, all experiments captured the sharp increase in soil moisture, but DA_ALL (the orange curve) reproduced both the peak (July 11) and the subsequent dry-down (July 12–13) with greater fidelity. At the non-Arctic grassland site (Figure 14b), the improvement derived from MWRI data is more prominent. The correlation in DA_ALL reached 0.43, compared to 0.23 for DA_L+C. MWRI demonstrates a strong capability in reproducing localized peaks in soil moisture, such as those on June 22 and June 27. It also well captures the three-wave variation characteristics of soil moisture during the period from June 27 to July 17, which constitutes a major reason for the significant increase in the correlation coefficient.

Formatted: Space Before: 1 line



745

Figure 14: Time series of daily mean soil moisture from model simulations, satellite retrievals, and in situ observations for different assimilation experiments. The green solid line represents in situ observations. Black, orange, and blue solid lines indicate soil moisture simulations from the control experiment, the DA_ALL assimilation experiment, and the DA_L+C assimilation experiment, respectively. Red dots, blue diamonds, and brown squares represent L- (SMAP), C- (ASCAT), and X-band (MWRI) satellite soil
750 **moisture products, respectively. Blue bars denote daily precipitation.**

4.2.2. Vegetation-based Observation Selection Strategy

The preceding analysis demonstrates that adding more satellite products does not necessarily lead to improved assimilation performance. A key to maximizing the benefit of multi-source data is to strategically select complementary combinations based on error characteristics. To this end, an additional experiment was conducted, referred to as the NEW experiment, which assimilates only SMAP and ASCAT soil moisture products over densely vegetated regions, and all three bands (SMAP, ASCAT, and MWRI) over sparsely vegetated regions (including bare soil, arctic grass, non-arctic grass, grass, corn, and wheat based on the CoLM classification). Figure 15 shows the probability density distribution of correlation coefficient differences relative to the CTL for the DA_NEW, DA_L+C, and DA_ALL experiments. The distributions for DA_L+C and DA_ALL are largely similar, indicating that the inclusion of MWRI (X-band) does not provide a clear advantage over the SMAP and ASCAT combination.

In contrast, the NEW experiment demonstrates a slight but constant improvement in performance. Its mean correlation improvement reaches 0.17, and its probability density in the high-positive range (0.6–0.75) is higher than that of DA_L+C and slightly higher than DA_ALL (see right inset of Figure 15). This indicates that the optimized combination in the NEW experiment improves both the stability and overall effectiveness of the assimilation system. Furthermore, in the negative difference range (–0.2 to –0.1), the NEW experiment shows substantially lower probability density than DA_ALL (see left inset), suggesting a reduced risk of performance degradation due to MWRI data in densely vegetated areas. These results confirm that the NEW experiment achieves superior assimilation performance by employing a more targeted multi-source data combination strategy. Although the magnitude of the enhancement is limited at this stage, this positive effect provides a preliminary validation of the potential of the synergistic assimilation scheme. This indicates that exploring the synergistic assimilation mechanisms of data from multiple sources can bring positive benefits to the model, representing a direction that warrants continued effort for the further optimization of soil moisture assimilation systems.

Formatted: Heading 3

Deleted: sensor

Deleted: .

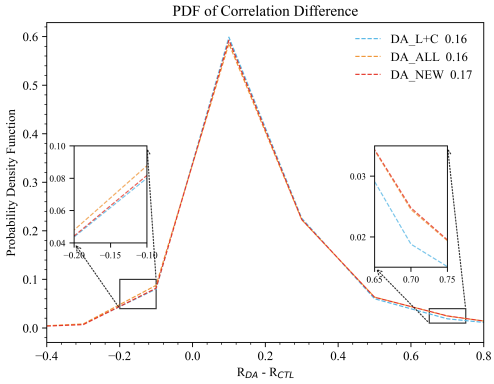


Figure 15: Probability density distributions of the correlation coefficient differences between assimilation experiments (NEW, DA_L+C, and DA_ALL) and the CTL, based on in situ observations.

To illuminate spatial heterogeneities in assimilation performance, we leverage existing in-situ networks to focus on two climatologically and ecologically distinct sub-regions of China: the central-west and the southeast. These areas exhibit contrasting vegetation characteristics—the former dominated by low-stature vegetation and bare ground, the latter by dense, high-biomass canopies—thereby providing a natural laboratory for evaluating spatially varying assimilation efficacy. In the CTL, correlation in the central-western region showed a north–south gradient, with a regional average of 0.25, whereas the southeastern region performed better, with an average correlation of 0.52. Data assimilation significantly improved soil moisture simulations in both regions. In the NEW experiment, the correlation in the central-western region increased to 0.5, with especially large improvements (often >0.5) in the north. The southeastern region also improved, with the average correlation rising to 0.58.

To comprehensively evaluate the specific contribution of the MWRI (X-band) product, this study employed a region-specific comparative strategy. In densely vegetated regions, where the assimilation weight of the X-band data is dynamically set to zero, the focus is on comparing the NEW experiment with the DA_ALL experiment. Conversely, in sparsely vegetated regions, the comparison primarily focuses on the differences between the NEW and DA_L+C experiments. Quantitative analysis reveals that in the sparsely vegetated central-western region of China, the inclusion of X-band data improved the correlation coefficient by 0.014. This improvement occurs because X-band microwave signals experience minimal canopy attenuation in low-biomass areas, allowing the retrievals to reliably capture surface soil moisture dynamics and provide valuable supplementary information. Meanwhile, in the densely vegetated region, the new assimilation scheme achieved a correlation improvement of 0.1 compared to the DA_ALL experiment. In such dense canopies, high-frequency X-band signals are strongly

Formatted: Space Before: 1 line

affected by vegetation, which increasing retrieval uncertainty. By dynamically masking these degraded observations, the adaptive scheme prevents the assimilation of erroneous data, thereby realizing this performance gain.

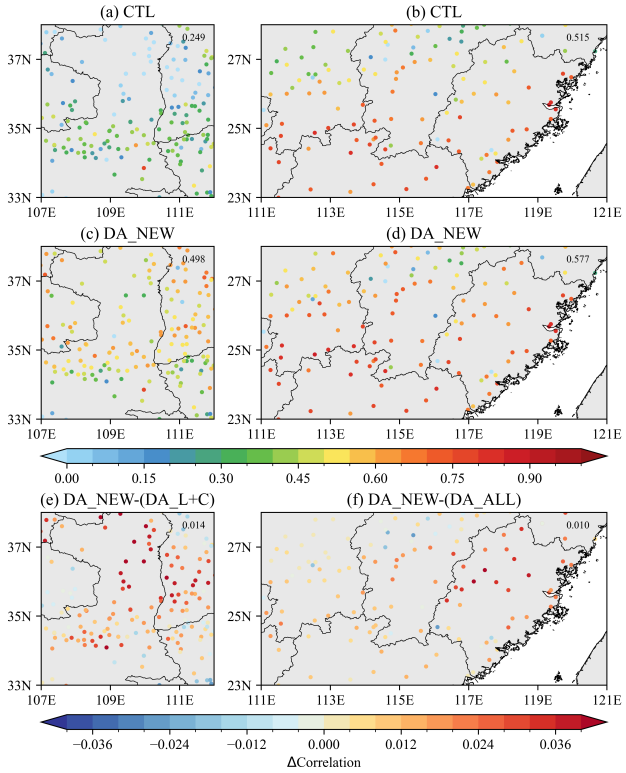


Figure 16: Spatial distribution of correlation coefficients between simulated and observed soil moisture. (a, b) show CTL results for central-west and southeast China, respectively, (c, d) show NEW experiment results for central-west and southeast China, respectively, and (e, f) show correlation differences between the NEW experiment and DA_L+C and between the NEW experiment and DA_ALL, respectively.

ubRMSE between modeled and observed soil moisture is shown in Figure 17. Compared to the CTL, the NEW experiment exhibited a remarkable reduction in ubRMSE in both regions. In central-western China, the ubRMSE decreased from 0.068 to

Formatted: Space Before: 1 line

0.058 m^3m^{-3}, and in southeastern China, it declined from 0.055 to 0.052 m^3m^{-3}. ubRMSE differences show predominantly negative values, indicating that the NEW scheme reduced model error across most areas. The spatial distribution of differences between the NEW experiment and the baselines (DA_L+C and DA_ALL) reveals negative values across most regions, indicating an overall ubRMSE reduction of approximately 0.001 m^3m^{-3}. Furthermore, compared to the improvements in correlation, the reduction in ubRMSE is relatively limited. However, localized increases in ubRMSE were also identified, indicating the need for further optimization strategies in multi-satellite data assimilation.

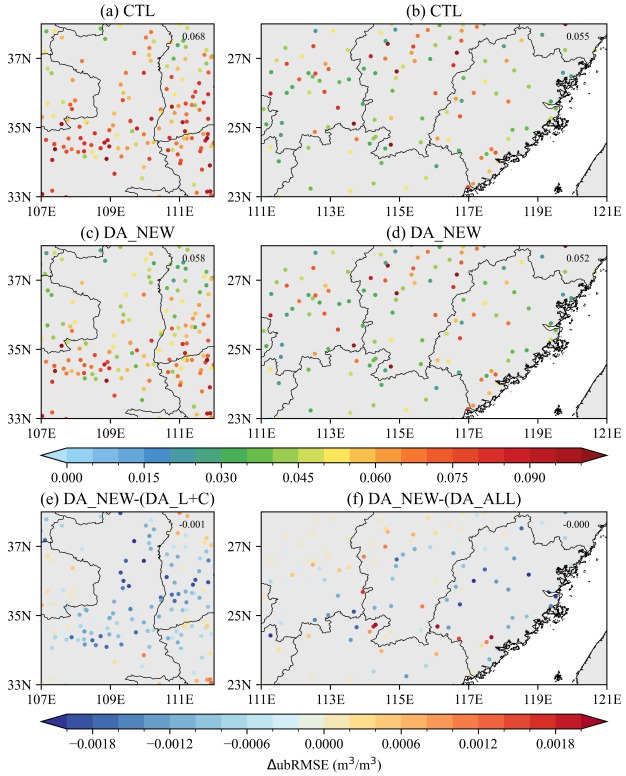


Figure 17: Same as Figure 16 except for ubRMSE.

4.2.3. Seasonal Applicability of the Optimized Strategy

To further investigate the differences in assimilation results across seasons, we extended the experiments to include spring (MAM), autumn (SON), and winter (DJF). Seasonal and intra-seasonal vegetation development can cause substantial changes in canopy conditions within the same vegetation type, complicating the assessment of X-band retrieval errors based on vegetation type alone. Figure 18 presents a comparison of the correlation coefficients between the DA_L+C and DA_ALL experiments across the four seasons for different vegetation types. The Non-arctic Grass and Corn regions exhibit more pronounced seasonal differences. In summer (JJA) and winter (DJF), the density of grasses and crops tends to stabilize. As a result, the mismatch between the vegetation correction and the actual canopy conditions is reduced, making the addition of the X-band more likely to result in positive effects. As shown in the figure, the orange bars are noticeably higher than the blue bars during summer and winter. Conversely, during the transitional phases of spring (MAM) and autumn (SON), the orange bars are lower than the blue bars, indicating that the inclusion of X-band data degrades the overall assimilation performance. This is likely because vegetation undergoes rapid growth or senescence during spring and autumn, accompanied by substantial changes in canopy structure and water content. As a result, X-band observations, which are more sensitive to vegetation effects, are more strongly influenced under these conditions. When vegetation dynamics are not adequately represented, X-band soil moisture retrieval errors may increase (Dash and Sinha, 2019; Stradiotti et al., 2025). These increased retrieval errors may reduce the benefit of assimilating X-band observations.

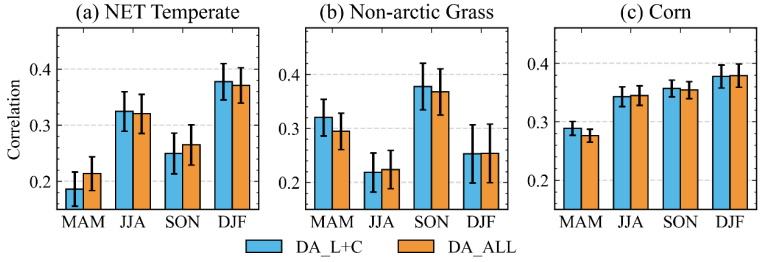


Figure 18: Comparison of assimilation performance for representative vegetation types across different seasons. The figure shows the correlation coefficients between simulated soil moisture and station observations for (a) NET Temperate, (b) Non-arctic Grass, and (c) Corn across the four seasons. The blue and orange bars represent the DA_L+C and DA_ALL experiments, respectively. Error bars indicate the 95% confidence intervals.

Based on the above analysis, the applicability of MWRI in multi-satellite assimilation is primarily determined by vegetation-induced observation uncertainties. When vegetation effects are weak and MWRI retrieval errors remain relatively small, X-band observations can provide complementary information and improve assimilation performance. Conversely, under dense or rapidly changing vegetation conditions, increased retrieval errors limit their contribution and may even degrade assimilation results.

Formatted: Heading 3

Formatted: Space Before: 1 line

Deleted: growth

Deleted: , or the vegetation density decreases significantly

Deleted: observation errors are relatively small and stable

Deleted: ¶

Deleted: drastic changes in morphological structure

Deleted: soil moisture retrievals may exhibit increased variability and occasional anomalous estimates, thereby increasing observation errors

Deleted: This elevated error uncertainty causes the assimilation of X-band data to be prone to negative impacts.

Deleted: Based on the above analysis, the winter settings follow those of summer, where X-band data is excluded only in dense vegetation areas. In spring and autumn, X-band data is not introduced in Corn and Non-arctic Grass. This is because Cron and Non-arctic Grass are undergoing rapid growth or senescence during the transitional phases of spring and autumn. The resulting substantial changes in vegetation morphology and water content are prone to enhancing X-band scattering noise and increasing observation uncertainty.¶

Figure 19 displays the PDF of the differences in correlation coefficients between the three sets of assimilation experiments and the control experiment based on in situ observations. As shown in Figure 19, the differences for all assimilation experiments are primarily distributed in the range greater than zero, indicating that assimilating satellite data produces a positive effect. The probability distribution of these differences reveals that improvements are more likely to occur during spring and autumn, where the probability of a correlation coefficient increment exceeding 0.5 is higher than in the other two seasons. In contrast, the assimilation improvement in winter is relatively small, with the magnitude of correlation coefficient increments mainly concentrated around 0.1.

Comparing the improvement effects of different assimilation experiments, it is evident that the DA_NEW experiment reduces the probability of negative effects across all seasons, shifting the overall probability density distribution toward the positive effect interval. Compared with the DA_ALL experiment, the improvements of the new scheme in spring, summer, and autumn are more concentrated around 0.3, while in winter, they are concentrated around 0.1. Furthermore, the mean correlation coefficients for each season indicate that the DA_NEW experiment produces higher average values than both the DA_L+C and DA_ALL experiments in every season. This demonstrates that the new scheme, by dynamically adjusting the combination of multi-source data, better integrates the advantages of multi-source observations, thereby improving global land surface assimilation performance.

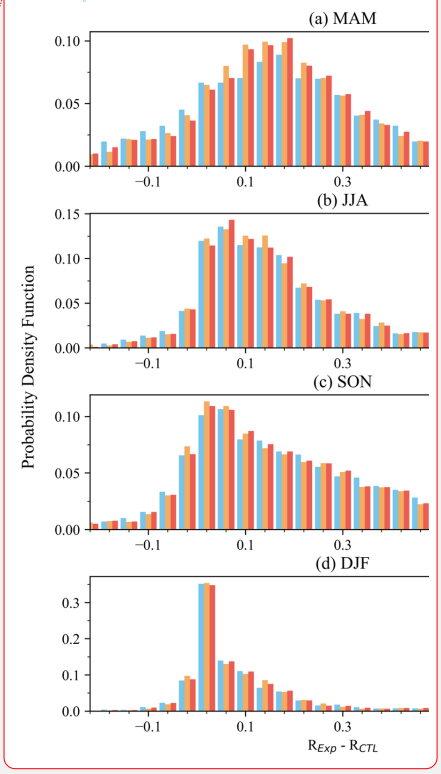
Formatted: Space Before: 1 line

Formatted: Font: (Asian) Times New Roman, English (US)

Formatted: Font: (Asian) Times New Roman, English (US)

Formatted: Font: (Asian) Times New Roman, English (US)

Deleted: ¶



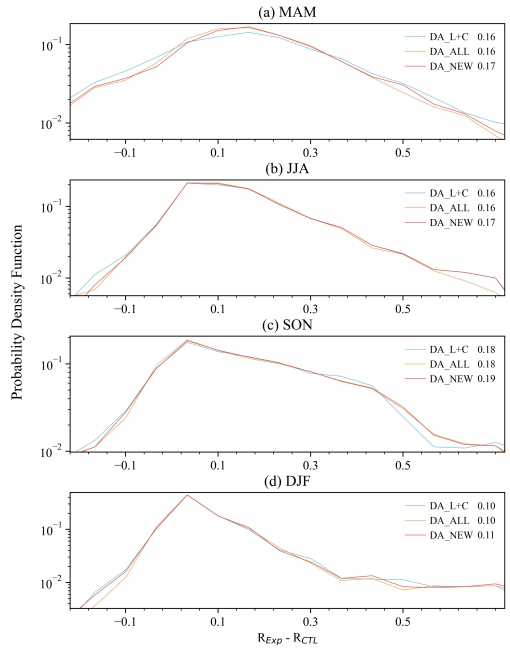


Figure 19: Seasonal variations in the probability density functions of the correlation coefficient differences between the assimilation experiments (DA_L+C, DA_ALL, and DA_NEW) and the control experiment based on station observations. (a) Spring (MAM), (b) Summer (JJA), (c) Autumn (SON), and (d) Winter (DJF). The numbers in the upper-right corner indicate the mean values.

5. Summary and Discussion

The effectiveness of assimilating satellite-based soil moisture retrievals in improving LSM performance has been widely recognized. With the rapid advancement of satellite remote sensing technology, numerous microwave radiometer-equipped polar-orbiting meteorological satellites have been launched globally, providing increasingly abundant observational resources. Against this background, effectively leveraging multi-source microwave data has become a key scientific challenge for enhancing land surface simulations. In this study, we develop a vegetation-adaptive framework for constructing optimal multi-satellite assimilation systems. Soil moisture retrievals from sensors operating at different microwave frequencies (SMAP L-band, ASCAT C-band, and MWRI X-band) were assimilated using the SEKF. In addition to performing a systematic

Formatted: English (US)

Formatted: Space Before: 1 line

evaluation of the performance across different frequency bands, we have attempted to establish an optimized scheme for multi-satellite synergistic assimilation based on the assessment results.

Experimental results indicate that assimilating satellite-retrieved soil moisture products improves near-surface soil-moisture simulations. The responses in deeper layers are presented as supplementary results and require further evaluation. However, the assimilation benefit does not monotonically increase with the amount of assimilated data. Analysis reveals that the performance of multi-satellite joint assimilation varies markedly across vegetation types. The dominant factor is that retrieval products exhibit vegetation-dependent errors, which mainly stem from the distinct vegetation penetration capabilities of radiation at different microwave bands. Therefore, careful observation screening based on error characteristics is critical to enhance multi-satellite joint assimilation. On the basis of assimilating SMAP and ASCAT retrieval products, this study proposes a vegetation-type-driven MWRI data selection scheme, which improves the overall performance of global multi-satellite joint assimilation.

But because no independent data assimilation spin-up was available, the system undergoes a transient adjustment after DA is activated. We note that, owing to the gradual downward redistribution of soil moisture within the soil column, the deeper soil layers adjust more slowly than the surface layer and may therefore require a longer assimilation spin-up period to reach full equilibrium.

While this study focused primarily on the role of vegetation density, other environmental factors such as terrain elevation, precipitation, and temperature can also influence the retrieval errors of different frequency bands. For instance, terrain-induced variations in local incidence angles can alter the polarization and scattering characteristics of microwave signals, thereby affecting retrieval accuracy (Gibon et al., 2024). Seasonal variations in vegetation cover, rainfall distribution, and temperature may also systematically impact retrieval performance (Liu et al., 2022). Future work should explore the influence of these factors through statistical or machine learning approaches to model their relationships with retrieval errors (Kim et al., 2023). Additionally, directly assimilating vegetation state variables offers another promising pathway beyond using vegetation solely for sensor selection. For instance, Zafarmomen et al. (2024) showed that assimilating Sentinel-derived leaf area index improves surface-groundwater interaction representation, suggesting that joint assimilation of soil moisture and vegetation indices could better constrain complex hydrological processes. Incorporating such models into multi-sensor assimilation frameworks may further enhance performance.

Finally, this study is based on offline land surface model simulations and does not account for land–atmosphere interactions, which may limit the generalizability of the proposed assimilation strategy in forecasting applications. Future studies should apply and evaluate the assimilation schemes within coupled land–atmosphere systems to better support improvements in weather and climate prediction.

Formatted: Default Paragraph Font, Font: (Default) Times New Roman, Font color: Auto

Deleted: The findings show that assimilating satellite soil moisture products significantly improves simulations of both surface and root-zone soil moisture.

Deleted: However, assimilation performance varies substantially with vegetation type. In densely vegetated regions, assimilating SMAP L-band retrievals consistently yields superior results due to the strong vegetation penetration capability of the L-band. In contrast, in sparsely vegetated high-latitude regions, MWRI (X-band) and ASCAT (C-band) products exhibit higher sensitivity to soil moisture variability and provide better assimilation outcomes. Vegetation-specific evaluation reveals that these differences stem from frequency-dependent vegetation penetration, which affects retrieval accuracy. ¶
Importantly, the results also demonstrate that increasing the number of assimilated satellite products does not always lead to improved performance. The combined assimilation of SMAP and ASCAT outperforms single-sensor assimilation. Further improvement is achieved only when MWRI data are selectively incorporated in regions with low vegetation cover. These results reveal that optimal sensor combination must be vegetation-adaptive. Accordingly, we developed a systematic framework that dynamically selects sensor combinations based on local vegetation conditions, prioritizing SMAP+ASCAT in most regions while conditionally adding MWRI only in sparse vegetation areas. This highlights that the effectiveness of multi-source assimilation depends not only on data volume but also on the complementarity of the assimilated information. ¶
B

Deleted: Surface soil moisture reaches a quasi-steady state within about 8 days, and the results for Days 1-61 are highly consistent with those for Days 8-61 (Figure S2). This consistency indicates that the initial adjustment does not affect the main conclusion regarding the relative assimilation skill of the different microwave bands for surface soil moisture.. However, w

Formatted: Font: (Asian) Times New Roman

Code and data availability. The exact version of the CoLM code (version 2014), the source code of the assimilation system, preprocessing scripts, model outputs, and input datasets actually used in this study (including the interpolated ERA5-Land da ta, the interpolated soil moisture observation datasets from SMAP, ASCAT, and FY-3D, as well as the selected 10 cm in-situ soil moisture data from ISMN) are archived in a trusted permanent repository at Zenodo under the following DOI: https://doi.org/10.5281/zenodo.18978246 (Bai, 2026).

Author contributions. Xuesong Bai: Writing – review & editing, Writing – original draft, Validation, Formal analysis, Conceptualization. Zhaohui Lin: Writing – review & editing, Supervision, Conceptualization. Zhengkun Qin: Writing – review & editing, Supervision, Conceptualization. Juan Li: Writing – review & editing, Methodology.

Competing interests. The contact author has declared that none of the authors has any competing interests.

Acknowledgements. We acknowledge the High Performance Computing Center of Nanjing University of Information Science & Technology for their support of this work. We acknowledge the use of ChatGPT for assistance with English translation and language polishing during manuscript preparation.

Financial support. This research was supported in part by Jianghuai Meteorological Joint Project of Anhui Natural Science Foundation under Grant 2408055UQ006, and in part by the National Natural Science Foundation of China under Grants U2442218 and 42375004, and in part by the Hainan Li'an Education, Science and Technology Innovation Unit Project under Grant ZDYF2025(LALH)005.

Deleted: Joint

References

Albergel, C., Munier, S., Leroux, D. J., Dewaele, H., Fairbairn, D., Barbu, A. L., Gelati, E., Dorigo, W., Faroux, S., Meurey, C., Le Moigne, P., Decharme, B., Mahfouf, J.-F., and Calvet, J.-C.: Sequential assimilation of satellite-derived vegetation and soil moisture products using SURFEX_v8.0: LDAS-Monde assessment over the Euro-Mediterranean area, Geosci. Model Dev., 10, 3889–3912, https://doi.org/10.5194/gmd-10-3889-2017, 2017.

Bai, X.: A Preliminary Study on a Synergistic Assimilation Scheme for Multi-band Satellite Soil Moisture Data, Zenodo [data set and code], https://doi.org/10.5281/zenodo.18978246, 2026.

Balsamo, G., Bouyssel, F., and Noilhan, J.: A simplified bi-dimensional variational analysis of soil moisture from screen-level observations in a mesoscale numerical weather-prediction model, Q. J. R. Meteorol. Soc., 130, 895–915, https://doi.org/10.1256/qj.02.215, 2004.

Bartalis, Z., Wagner, W., Naeimi, V., Hasenauer, S., Scipal, K., Bonekamp, H., Figa, J., and Anderson, C.: Initial soil moisture retrievals from the METOP-A Advanced Scatterometer (ASCAT), Geophys. Res. Lett., 34, https://doi.org/10.1029/2007GL031088, 2007.

Brocca, L., Moramarco, T., Melone, F., Wagner, W., Hasenauer, S., and Hahn, S.: Assimilation of surface- and root-zone ASCAT soil moisture products into rainfall-runoff modeling, IEEE Trans. Geosci. Remote Sens., 50, 2542–2555, https://doi.org/10.1109/TGRS.2011.2177468, 2012.

Formatted: Space After: 0.5 line

Formatted: Space Before: 1 line

Formatted

Carrera, M. L., Bélair, S., and Bilodeau, B.: Assimilation of passive L-band microwave brightness temperatures in the Canadian Land Data Assimilation System: Impacts on short-range warm season numerical weather prediction, J. Hydrometeor., 20, 1085–1105, https://doi.org/10.1175/JHM-D-18-0133.1, 2019.

Chambon, P., Mahfouf, J.-F., Audouin, O., Birman, C., Fourrié, N., Loo, C., Martet, M., Moll, P., Payan, C., Pourret, V., and Raspaud, D.: Global Observing System Experiments within the Météo-France 4D-Var Data Assimilation System, Mon. Wea. Rev., 151, 127–143, https://doi.org/10.1175/MWR-D-22-0087.1, 2023.

Chaubell, M. J., Yueh, S. H., Dunbar, R. S., Colliander, A., Chen, F., Chan, S. K., Entekhabi, D., Bindlish, R., O'Neill, P. E., Asanuma, J., Berg, A. A., Bosch, D. D., Caldwell, T., Cosh, M. H., Holifield Collins, C., Martínez-Fernández, J., Seyfried, M., Starks, P. J., Su, Z., Thibeault, M., and Walker, J.: Improved SMAP dual-channel algorithm for the retrieval of soil moisture, IEEE Trans. Geosci. Remote Sens., 58, 3894–3905, https://doi.org/10.1109/TGRS.2019.2959239, 2019.

Chen, F., Crow, W. T., Bindlish, R., Colliander, A., Burgin, M. S., Asanuma, J., and Aida, K.: Global-scale evaluation of SMAP, SMOS and ASCAT soil moisture products using triple collocation, Remote Sens. Environ., 214, 1–13, https://doi.org/10.1016/j.rse.2018.05.008, 2018.

Dai, Y., Zeng, X., Dickinson, R. E., Baker, I., Bonan, G. B., Bosilovich, M. G., Denning, A. S., Dirmeyer, P. A., Houser, P. R., Niu, G., Oleson, K. W., Schlosser, C. A., and Yang, Z.-L.: The Common Land Model, Bulletin of the American Meteorological Society, 84, 1013–1024, https://doi.org/10.1175/BAMS-84-8-1013, 2003.

Das, B., Rathore, P., Roy, D., Chakraborty, D., Bhattacharya, B. K., Mandal, D., Jatav, R., Sethi, D., Mukherjee, J., Sehgal, V. K., Singh, A. K., and Kumar, P.: Ensemble surface soil moisture estimates at farm-scale combining satellite-based optical-thermal-microwave remote sensing observations, Agric. For. Meteorol., 339, 109567, https://doi.org/10.1016/j.agrformet.2023.109567, 2023.

Dash, S. K. and Sinha, R.: A Comprehensive Evaluation of Gridded L-, C-, and X-Band Microwave Soil Moisture Product over the CZO in the Central Ganga Plains, India, Remote Sensing, 14, 1629, https://doi.org/10.3390/rs14071629, 2019.

de Rosnay, P., Drusch, M., Vasiljevic, D., Balsamo, G., Albergel, C., and Isaksen, L.: A simplified Extended Kalman Filter for the global operational soil moisture analysis at ECMWF, Quart J Royal Meteoro Soc., 139, 1199–1213, https://doi.org/10.1002/qj.2023, 2013.

Dorigo, W., Himmelbauer, I., Aberer, D., Schremmer, L., Petrakovic, I., Zappa, L., Preimesberger, W., Xaver, A., Annor, F., Ardö, J., Baldocchi, D., Bitelli, M., Blöschl, G., Bogena, H., Brocca, L., Calvet, J.-C., Camarero, J. J., Capello, G., Choi, M., Cosh, M. C., van de Giesen, N., Hajdu, I., Ikonen, J., Jensen, K. H., Kanniah, K. D., de Kat, I., Kirchengast, G., Kumar Rai, P., Kyrouac, J., Larson, K., Liu, S., Loew, A., Moghaddam, M., Martínez Fernández, J., Mattar Bader, C., Morbidelli, R., Musial, J. P., Osenga, E., Palecki, M. A., Pellarin, T., Petropoulos, G. P., Pfeil, I., Powers, J., Robock, A., Rüdiger, C., Rummel, U., Strobel, M., Su, Z., Sullivan, R., Tagesson, T., Varlagin, A., Vreugdenhil, M., Walker, J., Wen, J., Wenger, F., Wigneron, J. P., Woods, M., Yang, K., Zeng, Y., Zhang, X., Zreda, M., Dietrich, S., Gruber, A., van Oevelen, P., Wagner, W., Scipal, K., Drusch, M., and Sabia, R.: The International Soil Moisture Network: serving Earth system science for over a decade, Hydrol. Earth Syst. Sci., 25, 5749–5804, https://doi.org/10.5194/hess-25-5749-2021, 2021.

Dorigo, W., Wagner, W., Albergel, C., Albrecht, F., Balsamo, G., Brocca, L., Chung, D., Ertl, M., Forkel, M., Gruber, A., Haas, E., Hamer, P. D., Hirschi, M., Ikonen, J., de Jeu, R., Kidd, R., Lahoz, W., Liu, Y. Y., Miralles, D., Mistelbauer, T., Nicolai-Shaw, N., Parinussa, R., Pratola, C., Reimer, C., van der Schalie, R., Seneviratne, S. I., Smolander, T., and Lecomte, P.: ESA CCI Soil Moisture for improved Earth system understanding: State-of-the art and future directions, Remote Sens. Environ., 203, 185–215, https://doi.org/10.1016/j.rse.2017.07.001, 2017.

Draper, C. and Reichle, R.: The impact of near-surface soil moisture assimilation at subseasonal, seasonal, and inter-annual timescales, Hydrol. Earth Syst. Sci., 19, 4831–4844, https://doi.org/10.5194/hess-19-4831-2015, 2015.

Draper, C. S., Mahfouf, J.-F., and Walker, J. P.: An EKF assimilation of AMSR-E soil moisture into the ISBA land surface scheme, J. Geophys. Res., 114, D20104, https://doi.org/10.1029/2008JD011650, 2009.

Draper, C. S., Reichle, R. H., De Lannoy, G. J. M., and Liu, Q.: Assimilation of passive and active microwave soil moisture retrievals, Geophys. Res. Lett., 39, L04401, https://doi.org/10.1029/2011GL050655, 2012.

Drusch, M., Scipal, K., de Rosnay, P., Balsamo, G., Andersson, E., Bougeault, P., and Viterbo, P.: Towards a Kalman Filter based soil moisture analysis system for the operational ECMWF Integrated Forecast System, Geophys. Res. Lett., 36, L10401, https://doi.org/10.1029/2009GL037716, 2009.

Deleted: Dorigo, W. A., Scipal, K., Parinussa, R. M., Liu, Y. Y., Wagner, W., de Jeu, R. A. M., and Naeimi, V.: Error characterisation of global active and passive microwave soil moisture datasets, Hydrol. Earth Syst. Sci., 14, 2605–2616, https://doi.org/10.5194/hess-14-2605-2010, 2010.¶

El Hajj, M., Baghdadi, N., Zribi, M., and Bazzi, H.: Synergic Use of Sentinel-1 and Sentinel-2 Images for Operational Soil Moisture Mapping at High Spatial Resolution over Agricultural Areas, Remote Sensing, 9, 1292, https://doi.org/10.3390/rs9121292, 2017.

Entekhabi, D., Njoku, E. G., O'Neill, P. E., Kellogg, K. H., Crow, W. T., Edelstein, W. N., Entin, J. K., Goodman, S. D., Jackson, T. J., Johnson, J., Kimball, J., Piepmeier, J. R., Koster, R. D., Martin, N., McDonald, K. C., Moghaddam, M., Moran, S., Reichle, R., Shi, J. C., Spencer, M. W., Thurman, S. W., Tsang, L., and Van Zyl, J.: The Soil Moisture Active Passive (SMAP) Mission, Proc. IEEE, 98, 704–716, https://doi.org/10.1109/JPROC.2010.2043918, 2010.

Gibon, F., Mialon, A., Richaume, P., Rodríguez-Fernández, N., Aberer, D., Boresch, A., Crapolicchio, R., Dorigo, W., Gruber, A., Himmelbauer, I., Preimesberger, W., Sabia, R., Stradiotti, P., Tercjak, M., and Kerr, Y. H.: Estimating the uncertainties of satellite derived soil moisture at global scale, Science of Remote Sensing, 10, 100147, https://doi.org/10.1016/j.srs.2024.100147, 2024.

Girotto, M., Reichle, R. H., Rodell, M., Liu, Q., Mahanama, S., and De Lannoy, G. J.: Multi-sensor assimilation of SMOS brightness temperature and GRACE terrestrial water storage observations for soil moisture and shallow groundwater estimation, Remote Sens. Environ., 227, 12–27, https://doi.org/10.1016/j.rse.2019.03.040, 2019.

Gruber, A., Scanlon, T., van der Schalie, R., Wagner, W., and Dorigo, W.: Evolution of the ESA CCI Soil Moisture climate data records and their underlying merging methodology, Earth Syst. Sci. Data, 11, 717–739, https://doi.org/10.5194/essd-11-717-2019, 2019.

Herbert, C., de Rosnay, P., Weston, P., and Fairbairn, D.: Towards unified land data assimilation at ECMWF: Soil and snow temperature analysis in the SEKF, Quart J Royal Meteoro Soc, 150, 4133–4155, https://doi.org/10.1002/qj.4808, 2024.

Hersbach, H., Bell, B., Berrisford, P., Hirahara, S., Horányi, A., Muñoz‐Sabater, J., Nicolas, J., Peubey, C., Radu, R., Schepers, D., Simmons, A., Soci, C., Abdalla, S., Abellan, X., Balsamo, G., Bechtold, P., Biavati, G., Bidlot, J., Bonavita, M., De Chiara, G., Dahlgren, P., Dee, D., Diamantakis, M., Dragani, R., Flemming, J., Forbes, R., Fuentes, M., Geer, A., Haimberger, L., Healy, S., Hogan, R. J., Hólm, E., Janisková, M., Keeley, S., Laloyaux, P., Lopez, P., Lupu, C., Radnoti, G., de Rosnay, P., Rozum, I., Vamborg, F., Villaume, S., and Thépaut, J.: The ERA5 global reanalysis, Quart J Royal Meteoro Soc, 146, 1999–2049, https://doi.org/10.1002/qj.3803, 2020.

Hess, R.: Assimilation of screen-level observations by variational soil moisture analysis, Meteorol. Atmos. Phys., 77, 145–154, https://doi.org/10.1007/s007030170023, 2001.

Ji, D., Wang, L., Feng, J., Wu, Q., Cheng, H., Zhang, Q., Yang, J., Dong, W., Dai, Y., Gong, D., Zhang, R.-H., Wang, X., Liu, J., Moore, J. C., Chen, D., and Zhou, M.: Description and basic evaluation of Beijing Normal University Earth System Model (BNU-ESM) version 1, Geosci. Model Dev., 7, 2039–2064, https://doi.org/10.5194/gmd-7-2039-2014, 2014.

Kang, C. S., Zhao, T., Shi, J., Cosh, M. H., Chen, Y., Starks, P. J., Collins, C. H., Wu, S., Sun, R., and Zheng, J.: Global Soil Moisture Retrievals From the Chinese FY-3D Microwave Radiation Imager, IEEE Trans. Geosci. Remote Sens., 59, 4018–4032, https://doi.org/10.1109/TGRS.2020.3019408, 2020.

Kerr, Y. H., Waldteufel, P., Wigneron, J.-P., Delwart, S., Cabot, F., Boutin, J., Escorihuela, M.-J., Font, J., Reul, N., Gruhier, C., Juglea, S. E., Drinkwater, M. R., Hahne, A., Martín-Neira, M., and Mecklenburg, S.: The SMOS Mission: New Tool for Monitoring Key Elements ofthe Global Water Cycle, Proc. IEEE, 98, 666–687, https://doi.org/10.1109/JPROC.2010.2043032, 2010.

Kerr, Y. H., Waldteufel, P., Richaume, P., Wigneron, J. P., Ferrazzoli, P., Mahmoodi, A., Al Bitar, A., Cabot, F., Gruhier, C., Juglea, S. E., Leroux, D., Mialon, A., and Delwart, S.: The SMOS Soil Moisture Retrieval Algorithm, IEEE Trans. Geosci. Remote Sens., 50, 1384–1403, https://doi.org/10.1109/TGRS.2012.2184548, 2012.

Khaki, M., Hoteit, I., Kuhn, M., Forootan, E., and Awange, J.: Assessing data assimilation frameworks for using multi-mission satellite products in a hydrological context, Science of The Total Environment, 647, 1031–1043, https://doi.org/10.1016/j.scitotenv.2018.08.032, 2019.

Kim, H., Parinussa, R., Konings, A. G., Wagner, W., Cosh, M. H., Lakshmi, V., Zohaib, M., and Choi, M.: Global-scale assessment and combination of SMAP with ASCAT (active) and AMSR2 (passive) soil moisture products, Remote Sens. Environ., 204, 260–275, https://doi.org/10.1016/j.rse.2017.10.026, 2018.

Kim, H., Crow, W., Li, X., Wagner, W., Hahn, S., and Lakshmi, V.: True global error maps for SMAP, SMOS, and ASCAT soil moisture data based on machine learning and triple collocation analysis, Remote Sens. Environ., 298, 113776, https://doi.org/10.1016/j.rse.2023.113776, 2023.

Deleted: Jackson, T. J. and Schmugge, T. J.: Vegetation effects on the microwave emission of soils, Remote Sens. Environ., 36, 203–212, https://doi.org/10.1016/0034-4257(91)90057-D, 1991.¶

Kolassa, J., Reichle, R. H., and Draper, C. S.: Merging active and passive microwave observations in soil moisture data assimilation, Remote Sens. Environ., 191, 117–130, https://doi.org/10.1016/j.rse.2017.01.015, 2017.

Koster, R. D., Schubert, S. D., DeAngelis, A. M., Molod, A. M., and Mahanama, S. P.: Using a Simple Water Balance Framework to Quantify the Impact of Soil Moisture Initialization on Subseasonal Evapotranspiration and Air Temperature Forecasts, J. Hydrometeorol., 21, 1705–1722, https://doi.org/10.1175/JHM-D-20-0007.1, 2020.

Kumar, S. V., PETERSLIDARD, C., TIAN, Y., HOUSER, P., GEIGER, J., OLDEN, S., LIGHTY, L., EASTMAN, J., DOTY, B., and DIRMEYER, P.: Land information system: An interoperable framework for high resolution land surface modeling, Environ. Modell. Softw., 21, 1402–1415, https://doi.org/10.1016/j.envsoft.2005.07.004, 2006.

Kumar, S. V., Reichle, R. H., Koster, R. D., Crow, W. T., and Peters-Lidard, C. D.: Role of Subsurface Physics in the Assimilation of Surface Soil Moisture Observations, J. Hydrometeorol., 10, 1534–1547, https://doi.org/10.1175/2009JHM1134.1, 2009.

Kumar, S. V., Peters-Lidard, C. D., Mocko, D., Reichle, R., Liu, Y., Arsenault, K. R., Xia, Y., Ek, M., Riggs, G., Livneh, B., and Cosh, M.: Assimilation of Remotely Sensed Soil Moisture and Snow Depth Retrievals for Drought Estimation, J. Hydrometeorol., 15, 2446–2469, https://doi.org/10.1175/JHM-D-13-0132.1, 2014.

Lawrence, D. M., Fisher, R. A., Koven, C. D., Oleson, K. W., Swenson, S. C., Bonan, G., Collier, N., Ghimire, B., van Kampenhout, L., Kennedy, D., Kluzek, E., Lawrence, P. J., Li, F., Li, H., Lombardozzi, D., Riley, W. J., Sacks, W. J., Shi, M., Vertenstein, M., Wieder, W. R., Xu, C., Ali, A. A., Badger, A. M., Bisht, G., van den Broeke, M., Brunke, M. A., Burns, S. P., Buzan, J., Clark, M., Craig, A., Dahlin, K., Drewniak, B., Fisher, J. B., Flanner, M., Fox, A. M., Gentine, P., Hoffman, F., Keppel-Aleks, G., Knox, R., Kumar, S., Lenaerts, J., Leung, L. R., Lipscomb, W. H., Lu, Y., Pandey, A., Pelletier, J. D., Perket, J., Randerson, J. T., Ricciuto, D. M., Sanderson, B. M., Slater, A., Subin, Z. M., Tang, J., Thomas, R. Q., Val Martin, M., and Zeng, X.: The Community Land Model Version 5: Description of New Features, Benchmarking, and Impact of Forcing Uncertainty, J. Adv. Model. Earth Syst., 11, 4245–4287, https://doi.org/10.1029/2018MS001583, 2019.

Li, J., Qin, Z., Liu, G., and Huang, J.: Added Benefit of the Early-Morning-Orbit Satellite Fengyun-3E on the Global Microwave Sounding of the Three-Orbit Constellation, Adv. Atmos. Sci., 41, 39–52, https://doi.org/10.1007/s00376-023-2388-z, 2024.

Li, X., Chen, G., Liu, X., Liang, X., Wang, S., Chen, Y., Pei, F., and Xu, X.: A New Global Land-Use and Land-Cover Change Product at a 1-km Resolution for 2010 to 2100 Based on Human–Environment Interactions, Annals of the American Association of Geographers, 107, 1040–1059, https://doi.org/10.1080/24694452.2017.1303357, 2017.

Lievens, H., Reichle, R. H., Liu, Q., De Lannoy, G. J., Dunbar, R. S., Kim, S. B., Das, N. N., Cosh, M., Walker, J. P., and Wagner, W.: Joint Sentinel-1 and SMAP data assimilation to improve soil moisture estimates, Geophys. Res. Lett., 44, 6145–6153, https://doi.org/10.1002/2017GL073904, 2017.

Lin, L., Ebtehaj, A. M., Wang, J., and Bras, R. L.: Soil moisture background error covariance and data assimilation in a coupled land-atmosphere model, Water Resour. Res., 53, 1309–1335, https://doi.org/10.1002/2015WR017548, 2017.

Lin, Z., Liu, H., Xie, Z., Wang, A., and Liu, S.: The Curvelet Transform, Chinese Journal of Atmospheric Sciences, 27, 118–133, https://doi.org/10.3878/j.issn.1006-9895.2008.04.19, 2010.

Liu, D. and Mishra, A. K.: Performance of AMSR_E soil moisture data assimilation in CLM4.5 model for monitoring hydrologic fluxes at global scale, J. Hydrol., 547, 67–79, https://doi.org/10.1016/j.jhydrol.2017.01.036, 2017.

Liu, W., Wang, J., Xu, F., Li, C., and Xian, T.: Validation of Four Satellite-Derived Soil Moisture Products Using Ground-Based In Situ Observations over Northern China, Remote Sensing, 14, 1419, https://doi.org/10.3390/rs14061419, 2022.

Liu, Y., Peters-Lidard, C. D., Kumar, S., Foster, J. L., Shaw, M., Tian, Y., and Fall, G. M.: Assimilating satellite-based snow depth and snow cover products for improving snow predictions in Alaska, Adv. Water Res., 54, 208–227, https://doi.org/10.1016/j.advwatres.2013.02.005, 2013.

Mousa, B. G. and Shu, H.: Spatial Evaluation and Assimilation of SMAP, SMOS, and ASCAT Satellite Soil Moisture Products Over Africa Using Statistical Techniques, Earth Space Sci., 7, e2019EA000841, https://doi.org/10.1029/2019EA000841, 2020.

Muñoz-Sabater, J.: ERA5-Land hourly data from 1950 to present, Copernicus Climate Change Service (C3S) Climate Data Store (CDS) [data set], https://doi.org/10.24381/cds.e2161bac, 2019.

Njoku, E., Stacey, J., and Barath, F.: The Seasat scanning multichannel microwave radiometer (SMMR): Instrument description and performance, IEEE J. Ocean. Eng., 5, 100–115, https://doi.org/10.1109/JOE.1980.1145458, 1980.

Njoku, E. G. and Entekhabi, D.: Passive microwave remote sensing of soil moisture, J. Hydrol., 184, 101–129, https://doi.org/10.1016/0022-1694(95)02970-2, 1996.
Njoku, E. G., Jackson, T. J., Lakshmi, V., Chan, T. K., and Nghiem, S. V.: Soil moisture retrieval from AMSR-E, IEEE Trans. Geosci. Remote Sens., 41, 215–229, https://doi.org/10.1109/TGRS.2002.808243, 2003.
O'Neill, P. E., Bindlish, R., Chan, S., Chaubell, J., Colliander, A., Njoku, E., and Jackson, T.: Soil Moisture Active Passive (SMAP) Algorithm Theoretical Basis Document: Level 2 & 3 Soil Moisture (Passive) Data Products, Revision G, Jet Propulsion Laboratory, California Institute of Technology, JPL D-66480, 111 pp., 2021.
O'Neill, P., Chan, S., Njoku, E., Jackson, T., Bindlish, R., Chaubell, J., and Colliander, A.: SMAP enhanced L2 radiometer half-orbit 9 km EASE-grid soil moisture, version 6, NASA National Snow and Ice Data Center Distributed Active Archive Center [data set], https://doi.org/10.5067/BN36FXOMMC4C, 2023.
Paloscia, S., Pettinato, S., Santi, E., Notarnicola, C., Pasolli, L., and Reppucci, A.: Soil moisture mapping using Sentinel-1 images: Algorithm and preliminary validation, Remote Sens. Environ., 134, 234–248, https://doi.org/10.1016/j.rse.2013.02.027, 2013.
Parinussa, R. M., Holmes, T. R. H., Wanders, N., Dorigo, W. A., and de Jeu, R. A. M.: A Preliminary Study toward Consistent Soil Moisture from AMSR2, J. Hydrometeorol., 16, 932–947, https://doi.org/10.1175/JHM-D-13-0200.1, 2015.
Peng, J., Albergel, C., Balenzano, A., Brocca, L., Cartus, O., Cosh, M. H., Crow, W. T., Dabrowska-Zielinska, K., Dadson, S., Davidson, M. W. J., de Rosnay, P., Dorigo, W., Gruber, A., Hagemann, S., Hirschi, M., Kerr, Y. H., Lovergine, F., Mahecha, M. D., Marzahn, P., Mattia, F., Musial, J. P., Preuschmann, S., Reichle, R. H., Satalino, G., Silgram, M., van Bodegom, P. M., Verhoest, N. E. C., Wagner, W., Walker, J. P., Wegmüller, U., and Loew, A.: A roadmap for high-resolution satellite soil moisture applications – confronting product characteristics with user requirements, Remote Sens. Environ., 252, 112162, https://doi.org/10.1016/j.rse.2020.112162, 2021.
Piepmeier, J. R., Focardi, P., Horgan, K. A., Knuble, J., Ehsan, N., Lucey, J., Brambora, C., Brown, P. R., Hoffman, P. J., French, R. T., Mikhaylov, R. L., Kwack, E.-Y., Slimko, E. M., Dawson, D. E., Hudson, D., Peng, J., Mohammed, P. N., De Amici, G., Freedman, A. P., Medeiros, J., Sacks, F., Estep, R., Spencer, M. W., Chen, C. W., Wheeler, K. B., Edelstein, W. N., O'Neill, P. E., and Njoku, E. G.: SMAP L-Band Microwave Radiometer: Instrument Design and First Year on Orbit, IEEE Trans. Geosci. Remote Sens., 55, 1954–1966, https://doi.org/10.1109/TGRS.2016.2631978, 2017.
Reichle, R. H., Liu, Q., Koster, R. D., Crow, W. T., De Lannoy, G. J. M., Kimball, J. S., Ardizzone, J. V., Bosch, D., Colliander, A., Cosh, M., Kolassa, J., Mahanama, S. P., Prueger, J., Starks, P., and Walker, J. P.: Version 4 of the SMAP Level-4 Soil Moisture Algorithm and Data Product, J. Adv. Model. Earth Syst., 11, 3106–3130, https://doi.org/10.1029/2019MS001729, 2019.
Santanello, J. A., Kumar, S. V., Peters-Lidard, C. D., and Lawston, P. M.: Impact of Soil Moisture Assimilation on Land Surface Model Spinup and Coupled Land–Atmosphere Prediction, J. Hydrometeorol., 17, 517–540, https://doi.org/10.1175/JHM-D-15-0072.1, 2016.
Seneviratne, S. I., Corti, T., Davin, E. L., Hirschi, M., Jaeger, E. B., Lehner, I., Orlowsky, B., and Teuling, A. J.: Investigating soil moisture–climate interactions in a changing climate: A review, Earth Sci. Rev., 99, 125–161, https://doi.org/10.1016/j.earscirev.2010.02.004, 2010.
Seo, E., Lee, M.-I., and Reichle, R. H.: Assimilation of SMAP and ASCAT soil moisture retrievals into the JULES land surface model using the Local Ensemble Transform Kalman Filter, Remote Sens. Environ., 253, 112222, https://doi.org/10.1016/j.rse.2020.112222, 2021.
Shan, X., Steele-Dunne, S., Hahn, S., Wagner, W., Bonan, B., Albergel, C., Calvet, J.-C., and Ku, O.: Assimilating ASCAT normalized backscatter and slope into the land surface model ISBA-A-gs using a Deep Neural Network as the observation operator: Case studies at ISMN stations in western Europe, Remote Sens. Environ., 308, 114167, https://doi.org/10.1016/j.rse.2024.114167, 2024.
Shen, W., Lin, Z., Qin, Z., and Li, J.: Development and preliminary validation of a land surface image assimilation system based on the Common Land Model, Geosci. Model Dev., 17, 3447–3465, https://doi.org/10.5194/gmd-17-3447-2024, 2024.
Stradiotti, P., Gruber, A., Preimesberger, W., and Dorigo, W.: Accounting for seasonal retrieval errors in the merging of multi-sensor satellite soil moisture products, Science of Remote Sensing, 12, 100242, https://doi.org/10.1016/j.srs.2025.100242, 2025.
Taylor, C. M.: Detecting soil moisture impacts on convective initiation in Europe, Geophys. Res. Lett., 42, 4631–4638, https://doi.org/10.1002/2015GL064030, 2015.

Deleted: Owe, M., de Jeu, R., and Walker, J.: A methodology for surface soil moisture and vegetation optical depth retrieval using the microwave polarization difference index, IEEE Trans. Geosci. Remote Sens., 39, 1643–1654, https://doi.org/10.1109/36.942542, 2001.¶

Tian, J., Lu, H., Yang, K., Qin, J., Zhao, L., Zhou, J., Jiang, Y., and Ma, X.: Quick estimation of parameters for the land surface data assimilation system and its influence based on the extended Kalman filter and automatic differentiation, Sci. China Earth Sci., 66, 2546–2562, https://doi.org/10.1007/s11430-022-1180-8, 2023.

Wagner, W., Hahn, S., Kidd, R., Melzer, T., Bartalis, Z., Hasenauer, S., Figa-Saldana, J., de Rosnay, P., Jann, A., Schneider, S., Komma, J., Kubu, G., Brugger, K., Aubrecht, C., Züger, J., Gangkofner, U., Kienberger, S., Brocca, L., Wang, Y., Blöschl, G., Eitzinger, J., Steinnocher, K., Zeil, P., and Rubel, F.: The ASCAT soil moisture product: a review of its specifications, validation results, and emerging applications, Meteorol. Z., https://doi.org/10.1127/0941-2948/2013/0399, 2013.

Wanders, N., Karssenberg, D., de Roo, A., de Jong, S. M., Bierkens, M. F. P., Han, C., Brdar, S., and Kollet, S.: Response of Convective Boundary Layer and Shallow Cumulus to Soil Moisture Heterogeneity: A Large-Eddy Simulation Study, J. Adv. Model. Earth Syst., 11, 4305–4322, https://doi.org/10.1029/2019MS001772, 2019a.

Wanders, N., Karssenberg, D., de Roo, A., de Jong, S. M., and Bierkens, M. F. P.: The suitability of remotely sensed soil moisture for improving operational flood forecasting, Hydrol. Earth Syst. Sci., 18, 2343–2357, https://doi.org/10.5194/hess-18-2343-2014, 2019b.

Wigneron, J.-P., Jackson, T. J., O'Neill, P., De Lannoy, G., de Rosnay, P., Walker, J. P., Ferrazzoli, P., Mironov, V., Bircher, S., Grant, J. P., Kurum, M., Schwank, M., Munoz-Sabater, J., Das, N., Royer, A., Al-Yaari, A., Al Bitar, A., Fernandez-Moran, R., Lawrence, H., Mialon, A., Parrens, M., Richaume, P., Delwart, S., and Kerr, Y.: Modelling the passive microwave signature from land surfaces: A review of recent results and application to the L-band SMOS & SMAP soil moisture retrieval algorithms, Remote Sens. Environ., 192, 238–262, https://doi.org/10.1016/j.rse.2017.01.024, 2017.

Yao, P., Lu, H., Zhao, T., Wu, S., Peng, Z., Cosh, M. H., Jia, L., Yang, K., Zhang, P., and Shi, J.: A global daily soil moisture dataset derived from Chinese FengYun Microwave Radiation Imager (MWRI) (2010–2019), Sci. Data, 10, 133, https://doi.org/10.1038/s41597-023-02007-3, 2023.

Yuan, H., Dai, Y., Xiao, Z., Ji, D., and Shangguan, W.: Reprocessing the MODIS Leaf Area Index products for land surface and climate modelling, Remote Sensing of Environment, 115, 1171–1187, https://doi.org/10.1016/j.rse.2011.01.001, 2011.

Zafarmomen, N., Alizadeh, H., Bayat, M., Ehtiat, M., and Moradkhani, H.: Assimilation of sentinel-based leaf area index for modeling surface-ground water interactions in irrigation districts, Water Resour. Res., 60, e2023WR036080, https://doi.org/10.1029/2023WR036080, 2024.

Zapotocny, T. H., Jung, J. A., Le Marshall, J. F., and Treadon, R. E.: A Two-Season Impact Study of Satellite and In Situ Data in the NCEP Global Data Assimilation System, Wea. Forecasting, 22, 887–909, https://doi.org/10.1175/WAF1025.1, 2007.

Zhan, Y. and Lin, Z.: The relationship between June precipitation over mid-lower reaches of the Yangtze River basin and spring soil moisture over the East Asian monsoon region, Acta Meteorol. Sin., 25, 355–363, https://doi.org/10.1007/s13351-011-0310-6, 2011.

Zhan, Y., Z. Lin, F. Tian, M. Cao, and Y. Xu: The Spatio-Temporal Characteristics of Soil Moisture and Its Memory over Huaihe River Basin, Advances in Meteorological Science and Technology, 10, 87–96, https://doi.org/10.3969/j.issn.2095-1973.2020.05.014, 2020 (in Chinese).

Zhang, Y., Liang, S., Ma, H., He, T., Wang, Q., Li, B., Xu, J., Zhang, G., Liu, X., and Xiong, C.: Generation of global 1 km daily soil moisture product from 2000 to 2020 using ensemble learning, Earth Syst. Sci. Data, 15, 2055–2079, https://doi.org/10.5194/essd-15-2055-2023, 2002.

Zhao, T., Shi, J., Entekhabi, D., Jackson, T. J., Hu, L., Peng, Z., Yao, P., Li, S., and Kang, C. S.: Retrievals of soil moisture and vegetation optical depth using a multi-channel collaborative algorithm, Remote Sens. Environ., 257, 112321, https://doi.org/10.1016/J.RSE.2021.112321, 2021.

Zhou, J., Zuo, Z., Rong, X., Li, K., Zhang, J., Yang, K., and Wu, L.: The Role of Soil Moisture Feedbacks in Future Summer Temperature Change over East Asia, JGR Atmospheres, 124, 12034–12056, https://doi.org/10.1029/2018JD029670, 2019.

Zhou, J., Zuo, Z., and Rong, X.: Comparison of the effects of soil moisture and El Niño on summer precipitation in eastern China, Sci. China Earth Sci., 63, 267–278, https://doi.org/10.1007/s11430-018-9469-6, 2020.

Zhu, Y., Li, X., Pearson, S., Wu, D., Sun, R., Johnson, S., Wheeler, J., and Fang, S.: Evaluation of Fengyun-3C Soil Moisture Products Using In-Situ Data from the Chinese Automatic Soil Moisture Observation Stations: A Case Study in Henan Province, China, Water, 11, 248, https://doi.org/10.3390/w11020248, 2019.

Zribi, M.: Surface soil moisture estimation from the synergistic use of the (multi-incidence and multi-resolution) active microwave ERS Wind Scatterometer and SAR data, Remote Sens. Environ., 86, 30–41, https://doi.org/10.1016/S0034-4257(03)00065-8, 2003.